Rapid Identification of Neutralizing Antibodies

against SARS-CoV-2 Variants by mRNA Display

Shiho Tanaka[φ1], C. Anders Olson*[φ1], Christopher O. Barnes[φ2], Wendy Higashide[1], Marcos Gonzalez[1], Justin Taft[3,6,7], Ashley Richardson[3,4,5,6,7], Marta Martin-Fernandez[3,4,5,6,7], Dusan Bogunovic[3,4,5,6,7], Priyanthi N.P. Gnanapragasam[2], Pamela J. Bjorkman[2], Patricia Spilman[1], Kayvan Niazi[1], Shahrooz Rabizadeh[1], and Patrick Soon-Shiong*[1]

[φ]These authors contributed equally

*Corresponding authors: patrick@nantworks.com; anders.olson@immunitybio.com;

[1]ImmunityBio, Inc., 9920 Jefferson Blvd., Culver City, CA, 90232, USA

[2]Division of Biology and Biological Engineering, California Institute of Technology, 1200 East California Blvd., Pasadena, CA, 91125, USA

[3]Center for Inborn Errors of Immunity, [4]Department of Pediatrics, [5]Precision Immunology Institute, [6]Mindich Child Health and Development Institute, [7]Department of Microbiology, Icahn School of Medicine at Mount Sinai, 1 Gustave Lane, Levy Plaza, New York, NY 10029-5674, USA SPA

Abstract

The increasing prevalence of SARS-CoV-2 variants with the ability to escape existing humoral protection conferred by previous infection and/or immunization necessitates the discovery of broadly-reactive neutralizing antibodies (nAbs). Utilizing mRNA display, we identified a set of antibodies against SARS-CoV-2 spike (S) proteins and characterized the structures of nAbs that recognized epitopes in the S1 subunit of the S glycoprotein. These structural studies revealed distinct binding modes for several antibodies, including targeting of rare cryptic epitopes in the receptor-binding domain (RBD) of S that interacts with angiotensin-converting enzyme 2 (ACE2) to initiate infection, as well as the S1 subdomain 1. A potent ACE2-blocking nAb was further engineered to sustain binding to S RBD with the E484K and L452R substitutions found in multiple SARS-CoV-2 variants. We demonstrate that mRNA display is a promising approach for the rapid identification of nAbs that can be used in combination to combat emerging SARS-CoV-2 variants.

Introduction

The emergence of severe acute respiratory syndrome coronavirus 2 (SARS-CoV-2), the causative agent of the respiratory disease COVID-19, has resulted in a pandemic that brought the world to a standstill (Zhou et al., 2020). Despite the rapid development and success of vaccines and antibody therapies, ongoing SARS-CoV-2 antigenic drift has resulted in the emergence of variants that pose new threats (Davies et al., 2021; Plante et al., 2021; Yurkovetskiy et al., 2020). Various studies have shown that several of these variants have the ability to escape antibody neutralization mediated by antisera from recovered COVID-19 patients/vaccinated individuals or recombinant neutralizing antibodies (nAbs) developed as therapeutics (Cerutti et al., 2021; McCallum et al., 2021a; Suryadevara et al., 2021). Thus, along with modified vaccines to combat variants, there is an urgent need for development of prophylactic and therapeutic anti-viral drugs, including biologics such as nAbs, with sustained efficacy against SARS-CoV-2 variants.

The trimeric SARS-CoV-2 spike (S) glycoprotein serves as the fusion machinery for viral entry, and therefore represents the main target of nAbs (Brouwer et al., 2020; Cao et al., 2020; Robbiani et al., 2020). The SARS-CoV-2 S trimer utilizes the angiotensin-converting enzyme 2 (ACE2) as its host receptor (Hoffmann et al., 2020; Li et al., 2003; Zhou et al., 2020), through interactions with the receptor-binding domains (RBDs) located at the apex of the S trimer. The RBDs adopt either 'down' or 'up' conformations, with RBD binding to ACE2 facilitated only by the 'up' conformation (Kirchdoerfer et al., 2016; Li et al., 2019; Walls et al., 2016, 2020; Wrapp et al., 2020; Yuan et al., 2017). While the majority of potent anti-SARS-CoV-2 nAbs target the RBD and directly compete with ACE2 binding (Barnes et al., 2020a; Brouwer et al., 2020; Cao et al., 2020; Robbiani et al., 2020), recent studies have revealed nAbs that target the N-terminal domain (NTD) (Liu et al., 2020; McCallum et al., 2021b) and S2 stem helix (Zhou et al., 2021).

3

63   The structures of numerous monoclonal antibodies (mAbs) recognizing the RBD and NTD

64   have been characterized (Barnes et al., 2020b, 2020a; Baum et al., 2020; Brouwer et al., 2020;

65   Hansen et al., 2020; Pinto et al., 2020), enabling their classification based on shared epitopes and

66   neutralizing properties (Barnes et al., 2020b; Dejnirattisai et al., 2021; McCallum et al., 2021b;

67   Yuan et al., 2021). A subset of mAbs that recognize non-overlapping epitopes are in clinical

68   trials or have received emergency use authorization from the US Food and Drug Administration

69   (FDA) for the treatment and prevention of COVID-19 (Cathcart et al., 2021; Jones et al., 2021;

70   Weinreich et al., 2021). However, ongoing viral evolution and genetic drift has resulted in an

71   accumulation of mutations and/or deletions found in the S RBD and NTD that enhance affinity

72   of ACE2 binding and allow some variants to evade existing immunity (Cele et al., 2021; Tegally

73   et al., 2021). Thus, current emergency-authorized therapies developed early in the pandemic

74   based on the first-wave or 'A' strain S sequence could potentially be less effective against

75   emerging SARS-CoV-2 variants that harbor escape mutations mapped to their epitopes (Greaney

76   et al., 2021a, 2021b; Starr et al., 2020, 2021; Weisblum et al., 2020).

77   Here, we report our identification via mRNA display (Newton et al., 2020; Olson et al.,

78   2008; Roberts and Szostak, 1997; Takahashi et al., 2003) of a set of novel mAbs targeting

79   SARS-CoV-2 S, which we demonstrate neutralize both authentic and pseudoviral SARS-CoV-2

80   with $IC_{50}s$ between 0.076 – 7.0 µg/mL. Structural analysis revealed a subset of these nAbs

81   recognize RBD and NTD epitopes, including a rare, cryptic, cross-reactive RBD epitope.

82   Moreover, we characterize a weakly neutralizing antibody that recognizes the S1 subdomain 1

83   (SD1), providing insight into a unique class of antibodies that are infrequently found among

84   convalescent individuals (Zost et al., 2020a, 2020b) that can be utilized in the fight against

85   COVID-19. Finally, we describe the utility of mRNA display for rapid identification of variant-

4

86   resistant antibody clones. This powerful technique enabled the rapid selection of a discovered

87   SARS-CoV-2 nAb to extend its neutralizing capability to SARS-CoV-2 expressing the E484K

88   and L452R S RBD mutations found in multiple SARS-CoV-2 variants.

89   **Results**

90   **Identification of Anti-SARS-CoV-2 Spike Antibodies by mRNA Display**

91   We utilized mRNA display to identify mAbs targeting the S protein of SARS-CoV-2 and

92   discovered 10 novel VH/VL sequences that bind various domains on S (Table S1). S comprises

93   an N-terminal fragment known as S1, which further divides into the NTD, ACE2 RBD, small C-

94   terminal subdomains 1 and 2 (SD1 and SD2), and a C-terminal "S2" fragment (Figure 1A). Bio-

95   layer interferometry (BLI) kinetic analysis using recombinant SARS-CoV-2 RBD (residue 319-

96   541), RBD-SD1 (residue 319-591), S1 (residue 16-685), and S2 (residue 686-1213) proteins

97   revealed 3 antibodies bind the RBD (N-612-017, N-612-056, and N-612-074), 2 antibodies bind

98   the SD1 domain (N-612-004 and N-612-041), 2 antibodies bind the NTD (N-612-002 and N-

99   612-014), and 3 antibodies bind the S2 domain (N-612-007, N-612-044, and N-612-086) (Figure

100   1A-C). All 10 antibodies bind corresponding binding domains with low nM binding affinity (K_D)

101   (Figure 1B and Table S2), but apparent affinities are far superior ($K_D < 3$ pM) for S trimers

102   (Figure 1B and 1C, and Table S3). Among the 3 RBD binders, only N-612-017 showed

103   competition with ACE2 binding (Figure 1D).

104   To further map the binding regions of the 10 antibodies, we performed epitope binning

105   experiments using S1 and S2 fragments separately (Figure 1E). Two NTD binders blocked each

106   other but not RBD or SD1 binding antibodies. The 3 RBD binders competed with each other

107   (Figure 1E and F) despite N-612-017 being the only ACE2 blocker (Figure 1D). SD1 binders N-

108   612-004 and N-612-041 blocked each other, but only N-612-041 blocked N-612-074 (an RBD

109   binder) suggesting N-612-041 and N-612-074 have proximal or overlapping binding sites

110   (Figure 1E and 1F). Epitope binning using the S2 domain revealed N-612-007 and N-612-044

111   are non-competing whereas N-612-086 competes with both N-612-007 and N-612-044,

112   suggesting they all bind distinct epitopes on S2 (Figure 1E and 1F).

113   In addition, multiple biophysical assays were carried out to determine the developability of

114   all 10 antibodies (Table S4) (Jain et al., 2017). All 10 mAbs displayed low polyreactivity scores

115   by meso scale diagnostic (MSD) analysis and low self-interaction scores by BLI-clone self-

116   interaction (CSI) (Table S4). Eight of the mAb candidates exhibited low hydrophobicity in the

117   hydrophobic interaction column (HIC) chromatography while higher hydrophobicity was

118   observed for N-612-041 and N-612-074 (Table S4). N-612-041 also showed more rapid

119   aggregation in an accelerated stability assay system while the other 9 mAbs demonstrated long-

120   term stability (Table S4). Furthermore, all 10 mAbs exhibited desirable thermostability of Fab in

121   differential scanning fluorimetry (DSF) melting temperature (Tm) analysis, although N-612-044

122   exhibited heterogeneous characteristics in thermostability and hydrophobic interaction column

123   chromatography. Ultimately, 7 out of 10 antibodies displayed biophysical characteristics within

124   the acceptance criteria, indicating antibodies engineered by mRNA display can have favorable

125   developability.
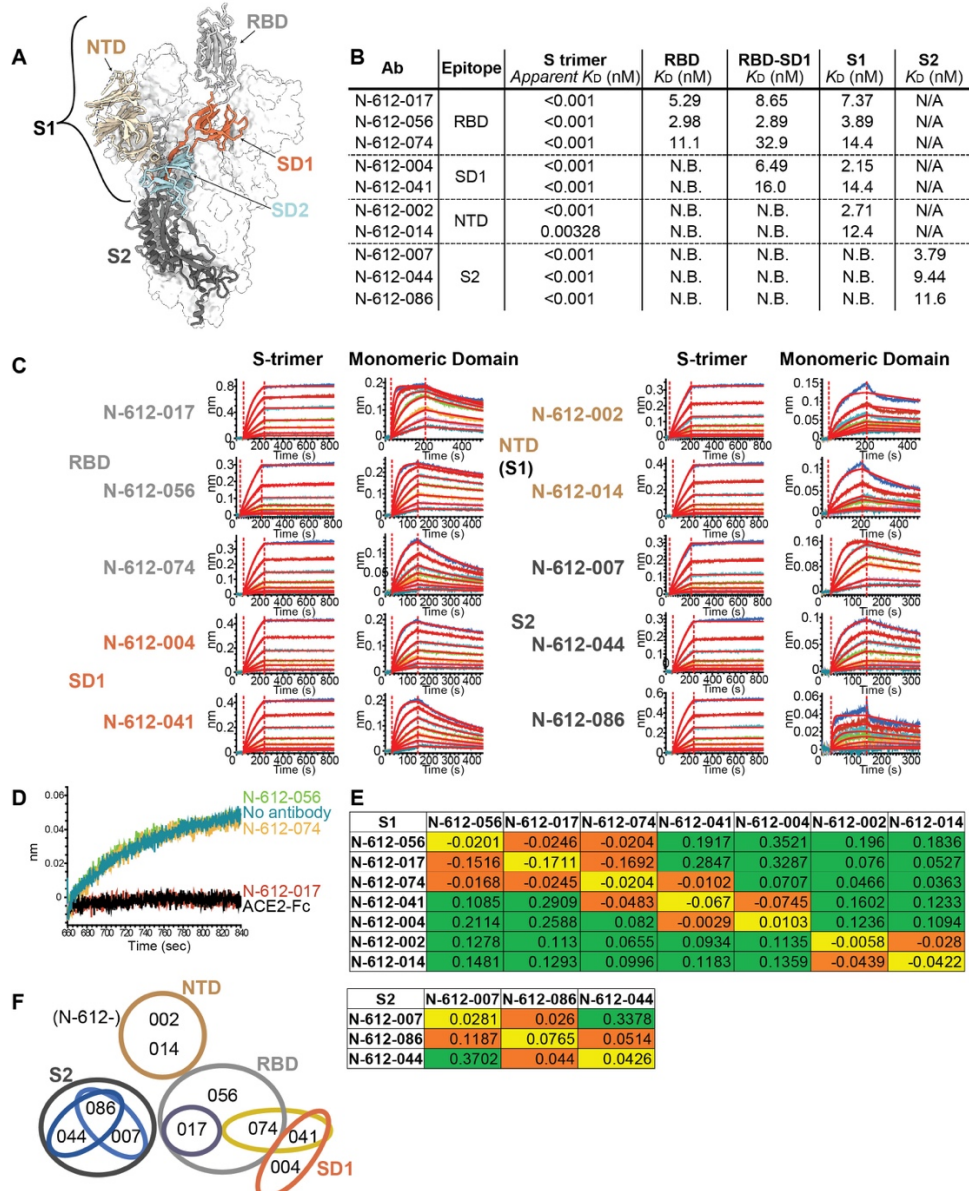
Figure 1. Identification of SARS-CoV-2 Spike Targeting Monoclonal Antibodies. (A) Model of the SARS-CoV-2 spike trimer domains (PDB 6VYB); NTD (wheat), RBD (light gray), SD1 (coral), SD2 (powder blue), and S2 (dark blue). (B) K_D summary table from BLI kinetic analysis of 10 antibodies against spike trimer and various domains used as analytes. N.B. indicates no binding. N/A is untested. Apparent K_D values for S-trimer were obtained by curve fitting with a bivalent model. (C) BLI kinetic analysis of 10 antibodies against the spike trimer (left) and each corresponding domain (right). (D) BLI blocking assay: biosensors were coated with RBD and subsequently all RBD binding antibodies (N-612-017, N-612-056, and N-612-074) and ACE2-IgG1Fc were incubated with RBD coated biosensor. The recorded signal from ACE2-IgG1Fc binding to the RBD on the biosensor indicates the RBD blocking capability of the test samples. Both N-612-017 and ACE2-IgG1Fc completely blocked RBD and ACE2 interaction. (E) Epitope binning data indicating competing antibody pairs in red and non-competing antibody pairs in green. Self-blocking is in orange. (F) Epitope binning diagram mapping overlapping regions of binding sites of 10 mAbs.

141   **Neutralization Activity Assessment of Anti-SARS-CoV-2 Antibodies**

142   Ten mAbs identified by mRNA display were assessed for neutralization activity against

143   authentic SARS-CoV-2 virus in a Vero E6 cell neutralization assay. The ACE2-blocking anti-

144   RBD antibody N-612-017 demonstrated the highest neutralization activity and the non-ACE2-

145   blocking RBD binder N-612-056 showed weaker but nearly complete neutralization of ~87%.

146   (Figure 2A). N-612-004 (SD1 binder), N-612-007 (S2 binder), and N-612-014 (NTD) antibodies

147   all showed some neutralization activity that plateaued at 40~60% (Figure 2A), similar to

148   previous observations made for anti-NTD antibodies (McCallum et al., 2021b). We next

149   investigated the activity of N-612-017 in combination with N-612-004, N-612-007, and N-612-

150   014. N-612-017 and respective partners were mixed in equal concentrations. All combinations

151   tested showed slightly improved IC_{50} values compared to N-612-017 by itself, suggesting both

152   antibodies present in mixture can bind to S simultaneously and in some cases non-RBD domain

153   binders can enhance activity of RBD-binding nAb (Figure 2B, C and D).
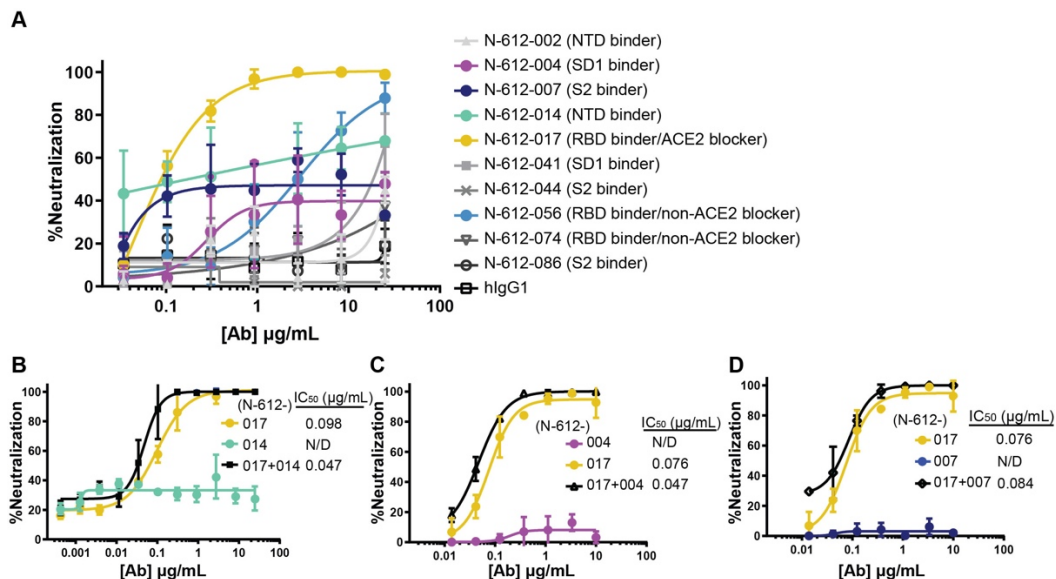
154
155   **Figure 2. Neutralization Activity of mAbs in Vero E6 Live Virus Neutralization Assay.** (A)
156   Dose-dependent neutralization of SARS-CoV-2 virus by 10 mAbs selected by mRNA library
157   display. N-612-017 neutralization activity in combination with (B) N-612-014, (C) N-612-004,
158   and (D) N-612-007. X-axis represents the concentration of antibodies when used alone; when
159   antibodies were combined, an equal concentration of each antibody was used.

160   Neutralization activity of N-612-014 (NTD binder) showed variable saturation between

161   assays and prevented accurate IC_{50} determination (Figure S1A). To test whether activity of N-

162   612-014 changes in time-dependent manner, we tested the effects of longer antibody-virus

163   incubation times on neutralization potency. With a virus-antibody incubation time of ~30 min,

164   neutralization activity plateaued between 20~90% (Figure S1A). In contrast, when virus was

165   incubated with antibody for 24 hours, neutralization activity plateaued at ~90% with IC_{50} values

166   of 0.023-0.025 µg/mL (Figure S1B). Longer incubation also resulted in improved neutralization

167   potencies for N-612-017, N-612-056, and positive control convalescent plasma serum (Figure

168   S1C), suggesting a change in viral infectivity due to a time-dependent conformational change in

169   spike (Huo et al., 2020; Wec et al., 2020).

170   **Structural Characterization of RBD-Specific, ACE2 Blocking nAb N-612-017**

171   To investigate the specificity of RBD-targeting for nAbs N-612-017 and N-612-056, we

172   determined a 3.2 Å single-particle cryo-electron microscopy (cryo-EM) structure of a complex

173   between SARS-CoV-2 S trimer and the N-612-017 Fab (Figure 3, Figure S2 and Table S5), and

174   a 2.9 Å X-ray crystal structure of a SARS-CoV-2 RBD – N-612-056 Fab complex (Figure 4 and

175   Table S6). The N-612-017 – S trimer complex structure revealed N-612-017 Fab binding to both

176   'up' and 'down' RBD conformations, and recognition of an epitope that partially overlapped

177   with the ACE2 receptor binding site (Figure 3A and 3B), consistent with BLI competition data

178   (Figure 1D). N-612-017 uses five of its six complementarity-determining region (CDR) loops

179   and HC framework region 3 (FWR3) to interact with an epitope focused on RBD residues

180   adjacent to the ACE2 receptor binding ridge (Figure 3C and 3D), resulting in ~1018$Å^2$ buried

181   surface area (BSA) on the epitope. The CDRH2 and CDRH3 loops mediate the majority of RBD

182   contacts (~616$Å^2$ of ~1030$Å^2$ total paratope BSA), establishing hydrophobic and hydrogen bond

183   interactions at the Fab-RBD interface. Of note, N-612-017 CDRH2 loop residues contact RBD

184   positions frequently mutated among circulating variants (Deng et al., 2021; Kuzmina et al., 2021;

185   McCallum et al., 2021a; Wang et al., 2021). RBD residue $E484_{RBD}$ established hydrogen bond

186   interactions with $G52_{HC}$ and $G54_{HC}$ in CDR2 and $D72_{HC}$ in FWR3 (Figure 3E), while $L452_{RBD}$

187   formed stacking interactions with CDR2 residue $Y52_{HC}$ (Figure 3F). Taken together, these data

188   indicate nAb N-612-017 targets the RBD similarly to nAbs that belong to the class 2 binding

189   mode, which is the predominant nAb class identified in convalescent and vaccinated donors

190   (Barnes et al., 2020b; Wang et al., 2021).
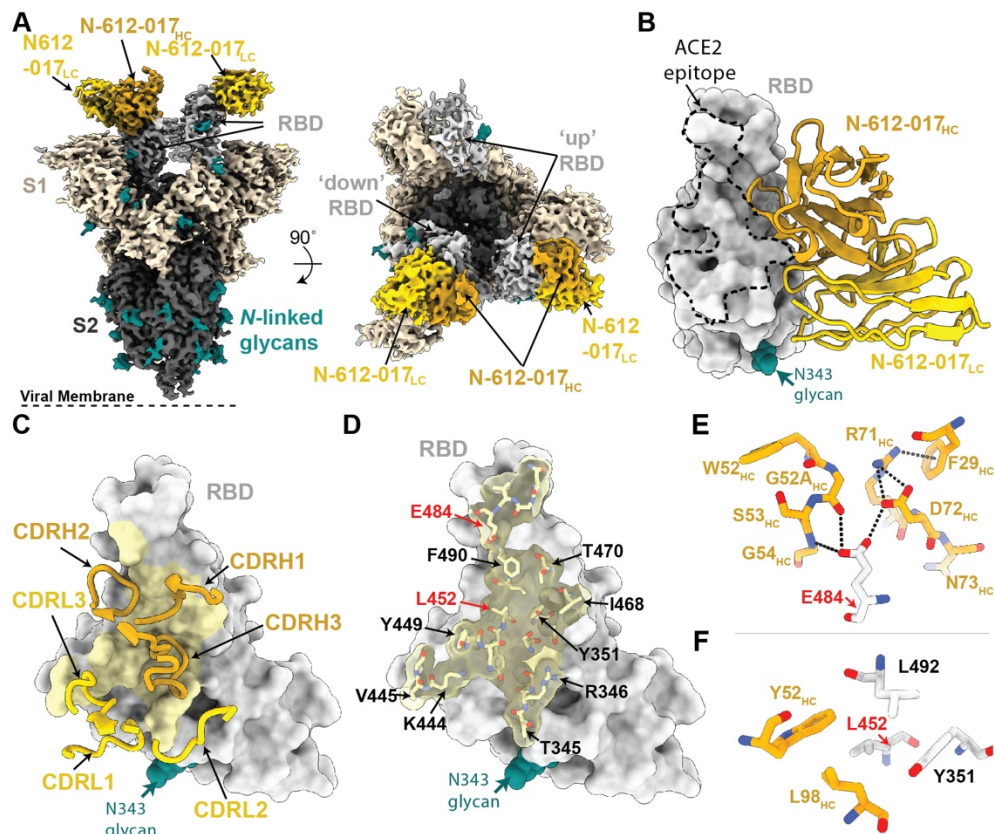
191
192   **Figure 3. Cryo-EM Structure of the N-612-017 – S Complex.** (A) Cryo-EM density for the N-
193   612-017- S trimer complex. Side view (left panel) illustrates orientation with respect to the viral
194   membrane (dashed line). (B) Close-up view of N-612-017 variable domains (HC: gold, LC:
195   yellow) bound to RBD (gray surface). ACE2 receptor binding site is shown as a dashed line. (C)
196   N-612-017 CDR loops mapped on the RBD. (D) Surface and stick representation of N-612-017
197   epitope (yellow) on RBD surface (gray). (E,F). Residue-level interactions between N-612-017
198   (gold) and SARS-CoV-2 RBD (gray). Potential hydrogen bond interactions are illustrated by
199   dashed black lines.

10

Structural Characterization of RBD-Specific nAb N-612-056 Targeting Cryptic Site

200

201   Next, we analyzed the high-resolution X-ray crystal structure of the SARS-CoV-2 RBD –N-

202   612-056 Fab complex (Figure 4A). This method was used rather than cryo-EM due to N-612-

203   056's lack of binding to intact S trimers (Figure 4A; inset). Similar to the donor-derived antibody

204   COVOX-45 (Dejnirattisai et al., 2021), N-612-056 binds a rare cryptic epitope that is not readily

205   found in the repertoire of antibodies from convalescent donors (Figure S4). Consistent with

206   observed binding to dissociated S1 protomers by single-particle cryo-EM (data not shown), the

207   N-612-056 cryptic epitope is inaccessible on an S trimer due to steric clashes with the

208   neighboring NTD, and does not overlap with the ACE2 binding site (Figure 4A and 4B). N-612-

209   056 HC and LC CDR loops participate equally to bury ~890 Å^2 of the RBD epitope surface area

210   that comprises residues 352-357 in the β1 strand, which is part of a structurally conserved 5-

211   stranded RBD β-sheet, and residues 457-471 that comprise a disordered loop directly beneath the

212   ACE2 receptor binding ridge (Figure 4C and 4D).

213   N-612-056 establishes a network of hydrogen bond and hydrophobic interactions that

214   include a stretch of hydrophobic residues in CDRH3 that mediate van der Waals interactions at

215   the RBD interface, and the formation of salt bridges between N-612-056 residues $D28_{LC}$ and

216     $E55_{LC}$ with $R346_{RBD}$ and $R357_{RBD}$, respectively (Figure 4E). These structural data explain the

217   observed cross-reactivity against SARS-CoV RBD (Figure S3A)(Cohen et al., 2021), as 14 of 20

218   epitope residues are strictly conserved and three additional residues (R346, R357 and K462

219   SARS-CoV-2 RBD numbering) are conservatively-substituted (K333, K344, and R449 SARS-

220   CoV RBD numbering) in SARS-CoV and SARS-CoV-2. (Figure 4F). Overall, these structural

221   data for the two RBD-targeting nAbs analyzed suggest comparable modes of recognition and

11

222   neutralization for antibodies N-612-017 and N-612-056, which were selected from mRNA

223   display, as those identified in convalescent or vaccinated donors.
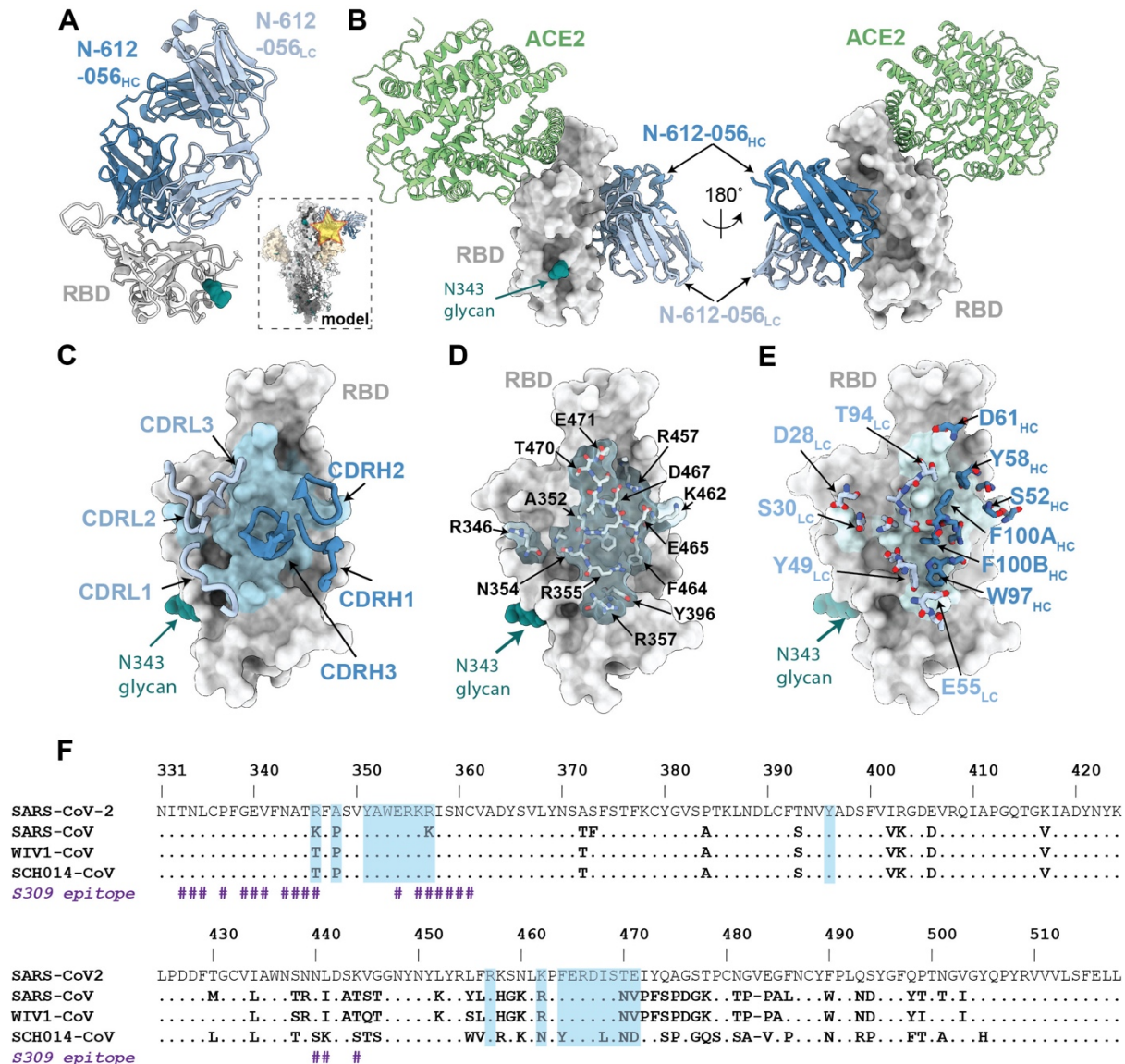
224

Figure 4. X-ray Crystal Structure of SARS-CoV-2 RBD in Complex with the N-612-056 Fab. (A) 2.9 Å X-ray crystal structure for the N-612-056 Fab – RBD complex. Inset: Overlay of the N-612-056-RBD crystal structure on a S trimer with 'up' RBD conformation (PDB 6VYB). (B) Composite model of N-612-056 – RBD (blue ribbon and gray surface, respectively) overlaid with soluble ACE2 (green, PDB 6M0J). The model was generated by aligning RBDs on 191 matched Cα atoms. (C) N-612-056 CDR loops (blue) mapped on the RBD surface (gray). The N-612-056 epitope is shown as a light blue surface. (D) Surface and stick representation of N-612-056 epitope. (E) N-612-056 paratope residues mapped on the RBD surface with epitope residues shown in light blue. (F) Sequence alignment of SARS-CoV-2, SARS-CoV, WIV1-CoV, and SCH014-CoV. N-612-056 epitope residues are shaded blue. S309 epitope residues are also shown (# symbol).

12

Structural Characterization of S1-Specific Antibodies N-612-014 and N-612-004

236

237   The primary target of SARS-CoV-2 nAbs is the viral spike glycoprotein, with the majority

238   of nAbs targeting the RBD (Greaney et al., 2021a; Piccoli et al., 2020). The S NTD represents a

239   common site of antigenic drift (Cele et al., 2021; McCarthy et al., 2021; Ribes et al., 2021), and

240   nAbs that bind to this region have recently been identified (Cerutti et al., 2021; McCallum et al.,

241   2021b; Suryadevara et al., 2021). To understand the binding mode of the NTD-targeting

242   antibody N-612-014 (Figure 1), we determined a 3.5Å cryo-EM structure of N-612-014 Fabs

243   complexed with stabilized S trimers (Figure 5A and Figure S2). N-612-014 adopted a binding

244   pose parallel to the viral membrane and primarily used HC CDR loops to recognize an epitope at

245   the periphery of the NTD (Figure 5A-C). The NTD epitope recognized by N-612-014 closely

246   resembles that recognized by the human-derived SARS-CoV-2 antibody S2X316 that targets

247   NTD antigenic site v, which resides outside of the antigenic supersite (site i) that is the main

248   target of neutralizing NTD antibodies (McCallum et al., 2021b). The N-612-014 epitope (~1070

249    $Å^2$ epitope BSA) involves contacts with peripheral loops comprising NTD residues 68-78, 175-

250   188, and 245-260, as well as contacts with the tip of the supersite β-hairpin (Figure 5D and 5E).

251   Despite contacts with residues 69-70$_{NTD}$ and 144$_{NTD}$, N-612-014 maintains binding to S trimers

252   of the B.1.1.7 lineage sequence (Figure S3), which has deletions at these positions that allow

253   escape from NTD supersite antibodies (McCallum et al., 2021b). These data suggest that N-612-

254   014 retains NTD binding capability and may retain potency in the presence of NTD mutations

255   commonly found in viral variants.

256   In addition to N-612-014, we also identified antibody N-612-004, an S1-specific antibody

257   that was mapped to a domain outside of the NTD and RBD (Figure 1). Using single-particle

258   cryo-EM, we determined a 4.8Å structure of N-612-004 bound to a dissociated S1 protomer,

13

259   which revealed recognition of a SD1 epitope (Figure 5F and Figure S2). Consistent with our

260   library design that varied CDR loops H2, H3 and L3, N-612-004 contacts were solely mediated

261   by these three regions, which led to recognition of loops 556-563 and 567-69 in the SD1 domain

262   (Figure 5G). The epitope for N-612-004 is not accessible on S trimers, which likely explains the

263   lack of N-612-004-like antibodies identified among a repertoire of antibodies found in

264   convalescent plasma (Figure S4).
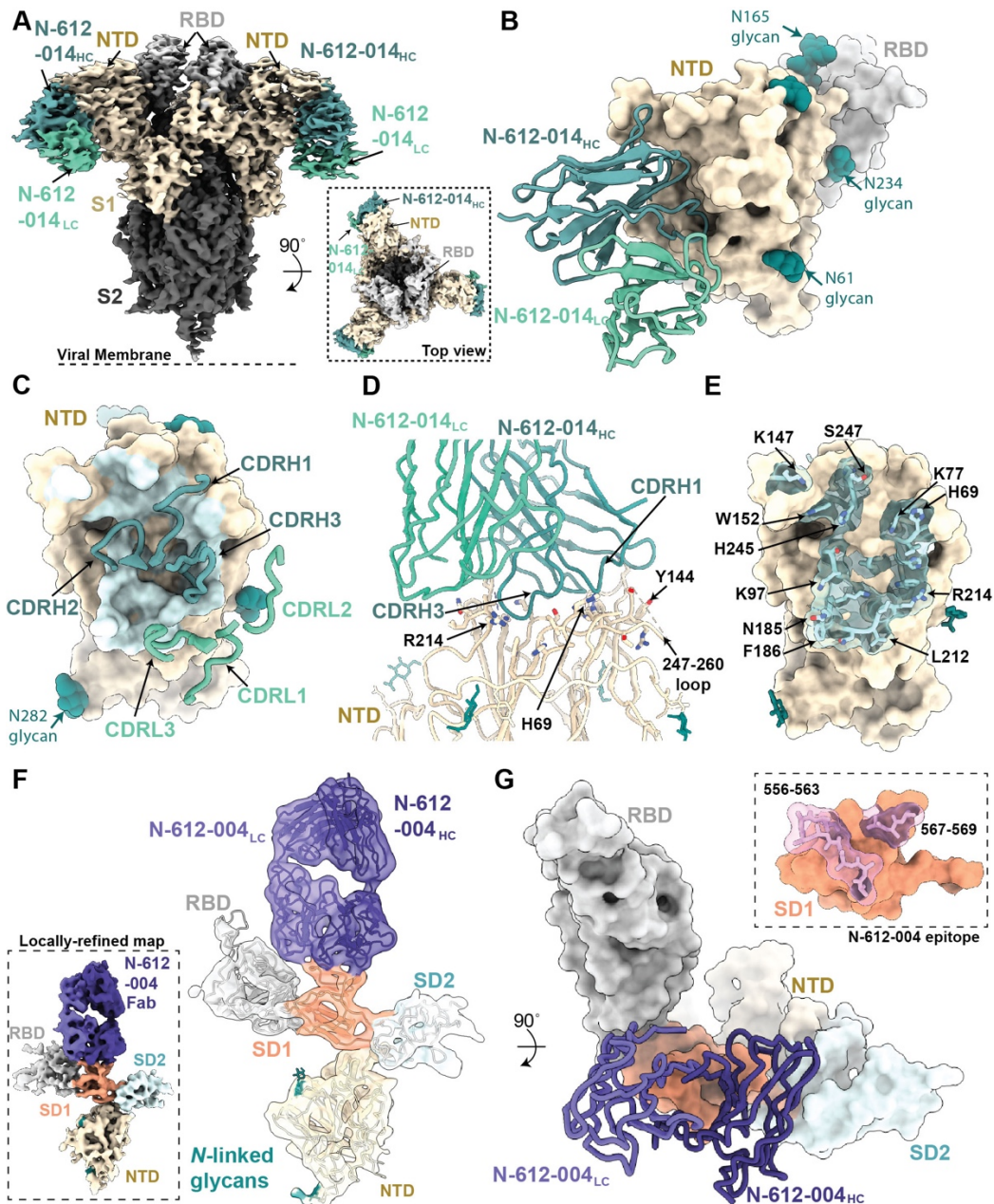
265

266 **Figure 5. Structures of S1-Specific Antibodies N-612-014 and N-612-004 Bound to SARS-**
267 **CoV-2 Spike.** (A) Cryo-EM structure of the N-612-014 – S trimer complex. Inset: top down
268 view of complex. (B) Close-up view of the N-612-014 variable domains (teal green) contacting
269 the NTD (tan surface). The RBD (gray surface) of an adjacent protomer is shown as reference.
270 (C) N-612-014 CDR loops (green ribbons) mapped onto the surface of the NTD (tan surface).
271 (D) Cartoon representation of the N-612-014 – NTD interface. (E) Surface and stick
272 representation of the N-612-014 epitope (light green surface). (F) Cryo-EM structure of the N-
273 612-004 – S1 protomer (inset) rigid body fit with individual S1 domains (cartoon). (G) Cartoon
274 and surface representation of N-612-004 (purple) recognition of the SD1 domain. Inset: N-612-
275 004 epitope (pink sticks) highlighted on the SD1 surface (orange). Given the low resolution,
276 epitope residues were assigned using a criterion of a distance of ≤7 Å between antibody-antigen
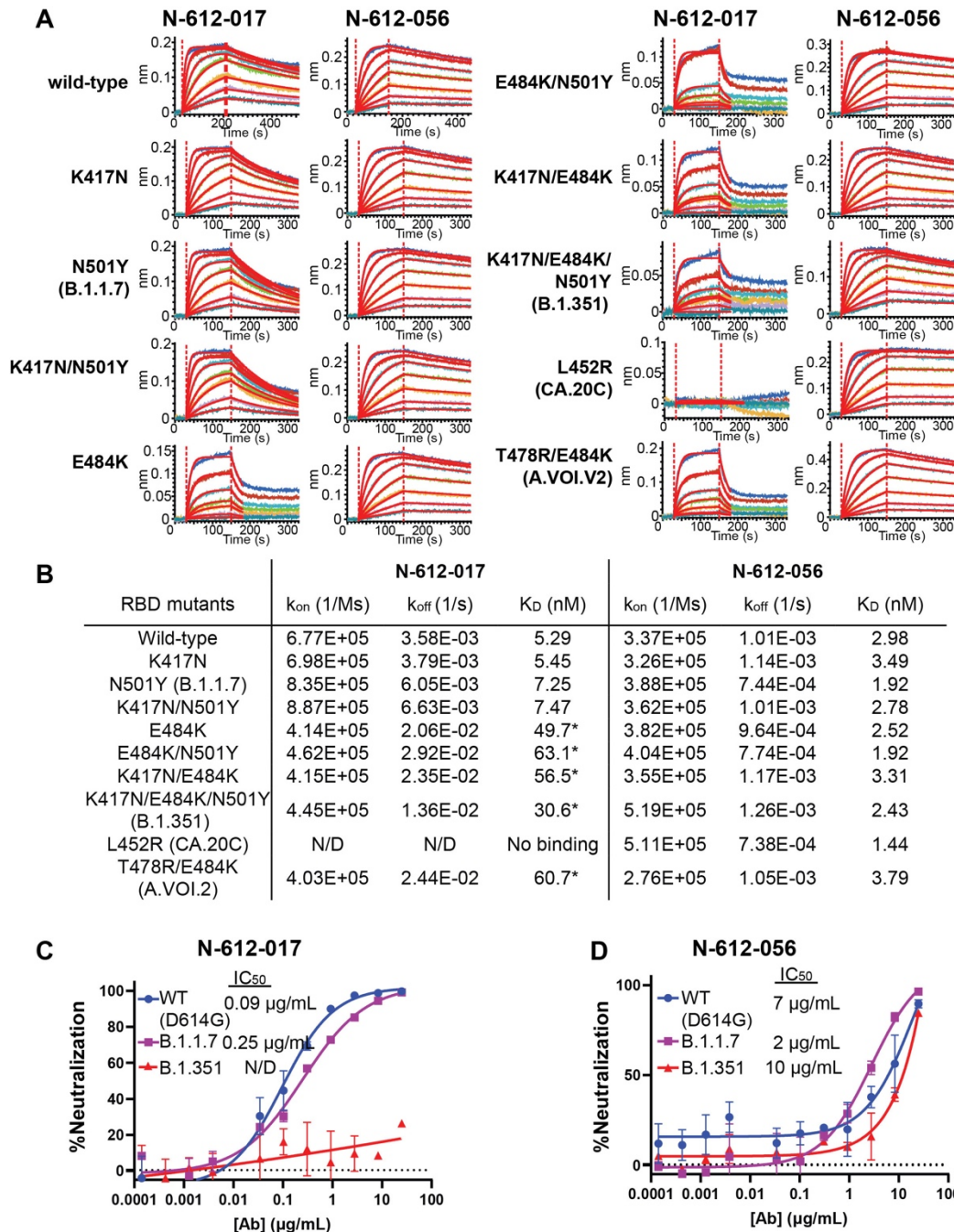277 Cα atoms.
278

279 **Activity of Identified nAbs Against Variants**

280 To assess the relative affinity of RBD-binding nAbs N-612-017 and N-612-056 against a

281 series of variants, BLI was performed using RBD variants B.1.1.7 (N501Y), B.1.351

282 (K417N/E484K/N501Y), CAL.20C (L452R), and A.VOI.V2(T478R/E484K) with single or

283 combined mutations. N-612-056 binding affinity was not affected by any of the RBD mutations

284 tested, which was anticipated based on structural characterization findings that indicate N-612-

285 056 recognizes a more conserved epitope on the surface of RBD. Neither N501Y (the only RBD

286 mutation in B.1.1.7 and one of 3 RBD mutations in B.1.351) nor K417N, (one of 3 RBD

287 mutations in B.1.351) disrupted the binding affinity of N-612-017. E484K - an escape mutant

288 found in many different variants, including B.1.351 and A.VOI.V2 (Oliveira et al., 2021; Tegally

289 et al., 2021; Weisblum et al., 2020) - did, however, reduce binding affinity of N-612-017 by 6-10

290 fold (Figure 6A and 6B). Furthermore, the L452R mutation found in CA.20C (also known as

291 B.1.1.427 and B.1.1.429) completely abolished the binding of RBD by N-612-017.

292 N-612-017 and N-612-056 were then evaluated in a pseudovirus neutralization assay

293 (Crawford et al., 2020) using wild-type (containing D614G), B.1.1.7, and B.1.351 pseudoviruses.

294 N-612-017 neutralized wild-type (D614G) and B.1.1.7 pseudoviruses with $IC_{50} = 0.09$-0.25

15

295   µg/mL but failed to neutralize B.1.351. N-612-056 retained neutralization activity against all

296   variants with IC$_{50}$ of 2-10 µg/mL as expected (Figure 6C).

297   The binding affinity of N-612-014 and N-612-004 against the recombinant S1 domain

298   containing B.1.1.7 mutations was tested and it was determined that 69-70del and Y144del on

299   NTD did not affect binding affinity of N-612-014 for S1 whereas these mutations moderately

300   lowered (by about 3-fold) the binding affinity of N-612-004 for S1 (Figure S3B and C).

B

RBD mutants	N-612-017			N-612-056		
	k_{on} (1/Ms)	k_{off} (1/s)	K_D (nM)	k_{on} (1/Ms)	k_{off} (1/s)	K_D (nM)
Wild-type	6.77E+05	3.58E-03	5.29	3.37E+05	1.01E-03	2.98
K417N	6.98E+05	3.79E-03	5.45	3.26E+05	1.14E-03	3.49
N501Y (B.1.1.7)	8.35E+05	6.05E-03	7.25	3.88E+05	7.44E-04	1.92
K417N/N501Y	8.87E+05	6.63E-03	7.47	3.62E+05	1.01E-03	2.78
E484K	4.14E+05	2.06E-02	49.7*	3.82E+05	9.64E-04	2.52
E484K/N501Y	4.62E+05	2.92E-02	63.1*	4.04E+05	7.74E-04	1.92
K417N/E484K	4.15E+05	2.35E-02	56.5*	3.55E+05	1.17E-03	3.31
K417N/E484K/N501Y (B.1.351)	4.45E+05	1.36E-02	30.6*	5.19E+05	1.26E-03	2.43
L452R (CA.20C)	N/D	N/D	No binding	5.11E+05	7.38E-04	1.44
T478R/E484K (A.VOI.2)	4.03E+05	2.44E-02	60.7*	2.76E+05	1.05E-03	3.79

301
302 **Figure 6. Binding Affinity and Neutralization Activity of N-612-017 and N-612-056 Against**
303 **Known SARS-CoV-2 Variants**. (A) BLI kinetic analysis of N-612-017 and N-612-056 affinity
304 against various mutations found in SARS-CoV-2 variants alone or in combination. N-612-017
305 binding curves against RBD mutants containing E484K were fit with 1:1 binding model using a
306 shorter dissociation time (30 sec) to highlight weakened binding. (B) Table of BLI kinetic assay
307 values. SARS-CoV-2 pseudovirus neutralization assay of antibodies. Asterisk indicates K_D
308 values obtained from processing the data with a shorter dissociation time to fit the curves to 1:1
309 binding and may not represent accurate K_D. (C) N-612-017 and (D) N-612-056 against wild-type
310 (D614G), B.1.1.7, and B.1.351 variants. Mean and standard deviation of duplicate experiments
311 (n=4), is shown.

17

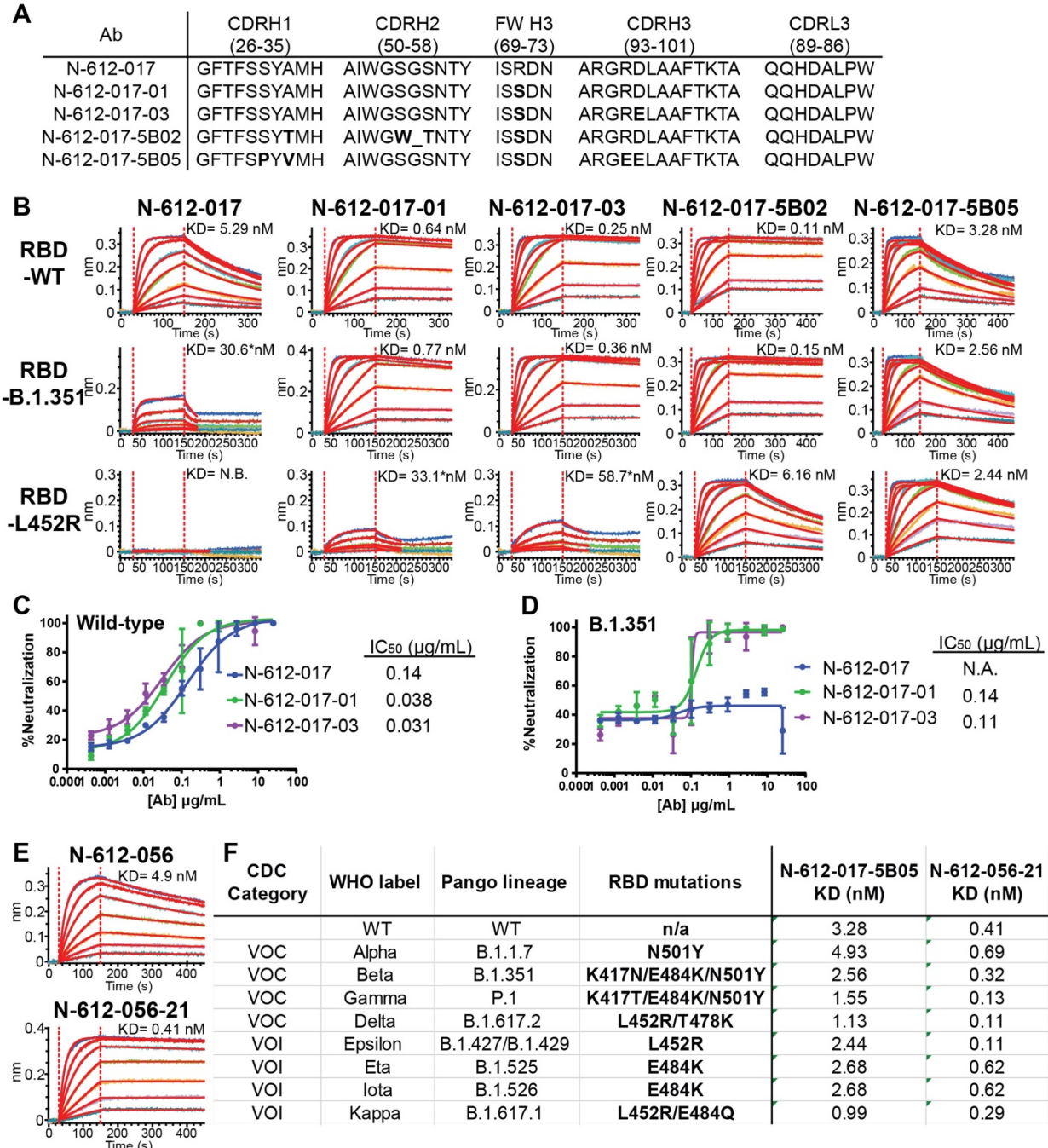312 **Generation of E484K and L452R-Resistant N-612-017**

313   To recover N-612-017 binding against RBD with the E484K substitution (RBD-E484K), we

314 used an mRNA-doped library for affinity maturation and identified mutations on VH framework

315 3 (Arg 71→ Ser) and CDR H3 (Asp 97→ Glu) that restored binding affinity against RBD-

316 E484K. The N-612-017 subclone N-612-017-01 containing a single VH:R71S mutation and

317 subclone N-612-017-03 containing double VH:R71S/D97E mutations were tested by BLI for

318 their binding of RBD-B.1.351 and RBD-L452R. Interestingly, both N-612-017-01 and N-612-

319 017-03 subclones not only exhibited restored binding affinity against E484K-expressing RBD

320 variants, they had 10- to 20-fold enhanced affinity against wild-type RBD (Figure 7A, 7B and

321 Table S7). While neither subclone displayed complete recovery of binding affinity against RBD-

322 L452R, affinity was relatively enhanced (K_D = 33.1-58.7 nM). These subclones were then tested

323 in a live virus neutralization assay against wild-type (D614G) and B.1.351 viruses and showed

324 neutralization activity against both, whereas the parent N-612-017 did not show neutralization

325 activity against B.1.351 (Figure 7C and 7D).

326   Subsequently, we used N-612-017-001 in affinity maturation against RBD-L452R and

327 identified 2 clones with restored affinity against RBD-L452R. N-612-017-5B02 containing 4

328 additional VH mutations (A33T/S54W/G54Δ/S55T) and N-612-017-5B05 containing 4

329 additional VH mutations (S31P/A33V/R96E/D97E) were tested by BLI for their binding of

330 B.1.351 and RBD-L452R. Both subclones showed complete recovery of binding affinity against

331 RBD-B.1.351 and RBD-L452R (Figure 7A, 7B, and Table S7).

332 **Affinity Maturation of N-612-056**

333   To improve potency of N-612-056, we utilized mRNA display for affinity maturation and

334   identified N-612-056-21 containing a single point mutation in VH CDR3 (Ser 99 → Pro) that

335   resulted in a 10-fold improvement in binding affinity (K_D= 0.41 nM) (Figure 7E).

336   Affinity matured N-612-017-5B05 and N-612-056-21 were tested against all the variants of

337   concern (VOC) and variants of interest (VOI) using BLI. N-612-017-5B05 showed binding

338   affinity to the variants that was similar to the parent molecule N-612-017, whereas N-612-056-21

339   displayed binding affinities improved as much as ~10-fold compared to N-612-056 (Figure 7F).

A

Ab	CDRH1 (26-35)	CDRH2 (50-58)	FW H3 (69-73)	CDRH3 (93-101)	CDRL3 (89-86)
N-612-017	GFTFSSYAMH	AIWGSGSNTY	ISRDN	ARGRDLAAFTKTA	QQHDALPW
N-612-017-01	GFTFSSYAMH	AIWGSGSNTY	IS**S**DN	ARGRDLAAFTKTA	QQHDALPW
N-612-017-03	GFTFSSYAMH	AIWGSGSNTY	IS**S**DN	ARGR**E**LAAFTKTA	QQHDALPW
N-612-017-5B02	GFTFSSY**T**MH	AIWG**W_T**NTY	IS**S**DN	ARGRDLAAFTKTA	QQHDALPW
N-612-017-5B05	GFTFS**PYV**MH	AIWGSGSNTY	IS**S**DN	ARG**EE**LAAFTKTA	QQHDALPW

B

C

D

E

F

CDC Category	WHO label	Pango lineage	RBD mutations	N-612-017-5B05 KD (nM)	N-612-056-21 KD (nM)
	WT	WT	n/a	3.28	0.41
VOC	Alpha	B.1.1.7	**N501Y**	4.93	0.69
VOC	Beta	B.1.351	**K417N/E484K/N501Y**	2.56	0.32
VOC	Gamma	P.1	**K417T/E484K/N501Y**	1.55	0.13
VOC	Delta	B.1.617.2	**L452R/T478K**	1.13	0.11
VOI	Epsilon	B.1.427/B.1.429	**L452R**	2.44	0.11
VOI	Eta	B.1.525	**E484K**	2.68	0.62
VOI	Iota	B.1.526	**E484K**	2.68	0.62
VOI	Kappa	B.1.617.1	**L452R/E484Q**	0.99	0.29

340
341 **Figure 7. Affinity Maturation of N-612-017 and N-612-056** (A) VH and VL sequences of N-
342 612-017 affinity matured subclones. (B) BLI kinetic analysis of N-612-017 affinity matured
343 subclones against RBD-wild-type, RBD-B.1.351, and RBD-L452R. Asterisk indicates K_D values
344 obtained from processing the data with a shorter dissociation time to fit the curves to 1:1 binding
345 model and may not represent accurate K_D values. SARS-CoV-2 live virus neutralization assay of
346 N-612-017, N-617-017-01, and N-612-017-03 against (C) wild-type and (D) B.1.351 variant.
347 Mean and standard deviation of duplicate experiments (n=3) (E) BLI kinetic analysis of N-612-
348 056 and affinity matured N-612-056-21 against RBD-wild-type. (F) Table of binding affinity of
349 N-612-017-5B05 and N-612-056-21 against RBD containing variant mutations from all the VOC
350 and VOI listed by CDC.

Discussion

351

352   Our use of *in vitro* mRNA display facilitated our identification of novel antibody sequences

353   and enabled us to enhance their binding affinity for mutated S of SARS-CoV-2 variants through

354   affinity maturation. BLI and epitope binning analysis determined that 10 unique IgG1 antibody

355   sequences identified here bind 7 distinct epitope regions on SARS-CoV-2 spike protein. Major

356   sequence differences in CDRH3 and CDRL3 loops in combination with minor variation in

357   CDRH1 and CDRH2 can drive the recognition of a broad spectrum of epitopes and create potent

358   neutralizing interactions with SARS-CoV-2 spike protein. Previous IGHV (immunoglobulin

359   heavy chain variable region) gene analysis identified distinct IGVH genes (e.g. 1-53) that were

360   more likely to produce potent RBD-binding nAbs (Dejnirattisai et al., 2021; Robbiani et al.,

361   2020; Yuan et al., 2020) within the human antibody repertoire. The nAb N-612-017 VH

362   sequence is most similar to IGHV 3-23, which are most abundant in human antibodies, and

363   shows potent neutralizing activity (< 0.1 μg/mL), suggesting CDR sequence variation is essential

364   in determining potency against antigen regardless of germline genes.

365   The majority of potent nAbs (~90%) are RBD targeting and the remainder target NTD of

366   spike protein (Brouwer et al., 2020; Cao et al., 2020; Liu et al., 2020; McCallum et al., 2021b).

367   Our most potent nAb N-612-017 is RBD targeting and categorized into Class 2 as characterized

368   by cryo-EM. Though N-612-056 also neutralized SARS-CoV-2 by targeting RBD, albeit at

369   lower potency, it lacks the ability to directly block ACE2 binding and binds to a cryptic epitope

370   on RBD. Similar antibody binding to this cryptic epitope by a patient-derived antibody has been

371   previously reported (Dejnirattisai et al., 2021). The rarity of this epitope is evident in the

372   convalescent plasma blocking assay, in which convalescent plasma from 3 out 4 patients failed

373   to block N-612-056 from binding to spike protein. This cryptic interface is well conserved, and

21

374   although the potency of N-612-056 is relatively low, cross-reactivity with SARS-CoV RBD and

375   sustained binding affinity for mutant SARS-CoV-2 RBD found in circulating variants suggests

376   N-612-056 may be an attractive monoclonal antibody therapy candidate against novel variants.

377   The cryo-EM structural data presented here reveal that N-612-014 binds NTD at a site

378   different from that of the majority of described antibodies (McCallum et al., 2021b), suggesting

379   the presence of a second neutralization site on the NTD. Proposed mechanisms for nAbs

380   targeting NTD include destabilization of S trimer by S1 shedding and blockage of cell-cell fusion

381   auxiliary receptor binding, membrane fusion, or proteolytic activation (Huo et al., 2020; Walls et

382   al., 2019; Wec et al., 2020; Wrobel et al., 2020). N-612-014 displayed neutralization activity in

383   live virus assays whereas it lacked neutralization activity in a pseudovirus assay. Although this

384   type of discrepancy is rare, such inter-assay discrepancies have been described previously (Liu et

385   al., 2020). N-612-014 may require a longer incubation time to reach maximum neutralization

386   because this allows the opportunity for the S trimer to adopt a conformation that is more

387   susceptible to S1 shedding that is promoted by the antibody, thus destabilizing spike; this

388   hypothesis awaits experimental confirmation.

389   The SD1-targeting antibody N-612-004 displayed partial neutralization activity and was

390   only observed in complex with S1 domain dissociated from the spike trimer in cryo-EM. To our

391   knowledge, there have been no reports on SD1-targeting antibodies that display neutralization

392   activity. We also identified the S2-targeting antibody N-612-007 that displayed partial

393   neutralization activity in a live virus neutralization assay and while structural analysis was

394   attempted, we were unable to visualize/characterize an S trimer/N-612-007 complex. nAbs

395   targeting S2 domain have been previously observed in MERS-CoV and SARS-CoV (Elshabrawy

396   et al., 2012; Lai et al., 2005; Lip et al., 2006; Pallesen et al., 2017), and recently reported

22

397　structures of SARS-CoV-2 S2/antibody complex have also revealed antibody binding to the S2

398　stem helix, which may interfere with membrane fusion machinary (Zhou et al., 2021). Other S2

399　epitope regions identified for SARS-CoV nAb are two heptad repeats region essential in cell

400　fusion during virus entry (Elshabrawy et al., 2012; Lip et al., 2006; Pallesen et al., 2017).

401　Neutralization activities of these non-RBD binders (N-612-014, N-612-004, and N-612-007)

402　were inconsistent between multiple assays and generally not very potent when tested

403　individually. However, when tested in combination with N-612-017, all slightly enhanced the

404　neutralization activity of N-612-017. This may suggest the role of non-RBD binding antibodies

405　in neutralization.

406　　　Bamlanivimab is a Class 2 RBD binder that neutralizes wild-type SARS-CoV-2 and was the

407　first antibody to attain emergency use authorization (EUA) by the FDA (Jones et al., 2021). This

408　EUA was, however, recently revoked due to loss of potency against SARS-CoV-2 variants

409　(Widera et al., 2021). Two alternate monoclonal antibody therapies remain available under EUA:

410　a combination of casirivimab plus imdevimab (Baum et al., 2020; Pinto et al., 2020) and

411　combination bamlanivimab plus etesevimab. In both cases, administering 2 monoclonal

412　antibodies together is key to compounding potency and reducing the risk of variant virus escape

413　from neutralization. Our N-612-017 antibody is a Class 2 RBD binder similar to bamlanivimab

414　that also displays a loss of activity in the presence of the E484K mutation. To address this

415　potential loss of efficacy, we used affinity maturation for N-612-017 and quickly identified

416　subclones that restored affinity for both E484K and L452R. N-612-056 is resistant to all the

417　RBD variants and N-612-014 is not affected by NTD mutation present in B.1.1.7. These nAbs

418　are attractive candidates for the use in combination with N-612-017. N-612-056 was quickly

23

419   affinity matured to present an attractive combo approach in combination with N-612-017 to

420   combat variants.

421   The recent emergence of more transmissible and infectious variants such as B.1.351 ('Beta')

422   and B.1.617 ('Delta') highlights the need for a method to rapidly address mutations that

423   overcome current therapies and existing immunity. The results described in this study

424   demonstrate the utility of mRNA display-based nAb discovery in the identification of antiviral

425   monoclonal antibodies against the rapidly evolving SARS-CoV-2 pathogen which should be

426   applicable to other novel or seasonal pathogens.

427

24

446

Author contributions

448   Experimental designs: C.A.O., S.T, C.O.B, K.N., S.R., and P.S.S; mRNA library display:

449   C.A.O; Cloning: C.A.O and W.H.; Protein Expression and Purification: C.A.O., S.T. and M.G.;

450   Kinetic Analysis, ACE2 Blocking Assay, Epitope Binning, and ELISA ACE2 blocking assay:

451   S.T., cryo-EM and X-ray crystallography: C.O.B and P.J.B.; Vero E6 Live Virus Neutralization

452   Assay: J.T., A.R., M.M.F. and D.B.; pseudo-typed virus neutralization assay: P.G.. Manuscript

453   preparation: S.T., C.O.B., C.A.O., and P.S..

454

Declaration of interests

456   C.A.O., S.T., W.H., K.N., and P.S.S. are inventors for an international patent application with

457   this work.

458

459

References

461 Adams, P.D., Afonine, P.V., Bunkóczi, G., Chen, V.B., Davis, I.W., Echols, N., Headd, J.J., Hung, L.-
462 W., Kapral, G.J., Grosse-Kunstleve, R.W., et al. (2010). PHENIX: a comprehensive Python-based
463 system for macromolecular structure solution. Acta Crystallogr. D Biol. Crystallogr. *66*, 213–221.

464 Barnes, C.O., West, A.P., Huey-Tubman, K.E., Hoffmann, M.A.G., Sharaf, N.G., Hoffman, P.R.,
465 Koranda, N., Gristick, H.B., Gaebler, C., Muecksch, F., et al. (2020a). Structures of Human
466 Antibodies Bound to SARS-CoV-2 Spike Reveal Common Epitopes and Recurrent Features of
467 Antibodies. Cell *182*, 828-842.e16.

468 Barnes, C.O., Jette, C.A., Abernathy, M.E., Dam, K.-M.A., Esswein, S.R., Gristick, H.B., Malyutin,
469 A.G., Sharaf, N.G., Huey-Tubman, K.E., Lee, Y.E., et al. (2020b). SARS-CoV-2 neutralizing
470 antibody structures inform therapeutic strategies. Nature *588*, 682–687.

471 Baum, A., Fulton, B.O., Wloga, E., Copin, R., Pascal, K.E., Russo, V., Giordano, S., Lanza, K.,
472 Negron, N., Ni, M., et al. (2020). Antibody cocktail to SARS-CoV-2 spike protein prevents rapid
473 mutational escape seen with individual antibodies. Science *369*, 1014–1018.

474 Bell, J.M., Chen, M., Baldwin, P.R., and Ludtke, S.J. (2016). High resolution single particle
475 refinement in EMAN2.1. Methods *100*, 25–34.

476 Brouwer, P.J.M., Caniels, T.G., Straten, K. van der, Snitselaar, J.L., Aldon, Y., Bangaru, S., Torres,
477 J.L., Okba, N.M.A., Claireaux, M., Kerster, G., et al. (2020). Potent neutralizing antibodies from
478 COVID-19 patients define multiple targets of vulnerability. Science *369*, 643–650.

479 Cao, Y., Su, B., Guo, X., Sun, W., Deng, Y., Bao, L., Zhu, Q., Zhang, X., Zheng, Y., Geng, C., et al.
480 (2020). Potent Neutralizing Antibodies against SARS-CoV-2 Identified by High-Throughput
481 Single-Cell Sequencing of Convalescent Patients' B Cells. Cell *182*, 73-84.e16.

482 Cathcart, A.L., Havenar-Daughton, C., Lempp, F.A., Ma, D., Schmid, M.A., Agostini, M.L.,
483 Guarino, B., Iulio, J.D., Rosen, L.E., Tucker, H., et al. (2021). The dual function monoclonal
484 antibodies VIR-7831 and VIR-7832 demonstrate potent in vitro and in vivo activity against SARS-
485 CoV-2. BioRxiv 10.1101/2021.03.09.434607.

486 Cele, S., Gazy, I., Jackson, L., Hwa, S.-H., Tegally, H., Lustig, G., Giandhari, J., Pillay, S., Wilkinson,
487 E., Naidoo, Y., et al. (2021). Escape of SARS-CoV-2 501Y.V2 from neutralization by convalescent
488 plasma. Nature *593*, 142–146.

489 Cerutti, G., Guo, Y., Zhou, T., Gorman, J., Lee, M., Rapp, M., Reddem, E.R., Yu, J., Bahna, F.,
490 Bimela, J., et al. (2021). Potent SARS-CoV-2 neutralizing antibodies directed against spike N-
491 terminal domain target a single supersite. Cell Host Microbe *29*, 819-833.e7.

492 Cohen, A.A., Gnanapragasam, P.N.P., Lee, Y.E., Hoffman, P.R., Ou, S., Kakutani, L.M., Keeffe, J.R.,
493 Wu, H.-J., Howarth, M., West, A.P., et al. (2021). Mosaic nanoparticles elicit cross-reactive
494 immune responses to zoonotic coronaviruses in mice. Science *371*, 735–741.

26

495   Crawford, K.H.D., Eguia, R., Dingens, A.S., Loes, A.N., Malone, K.D., Wolf, C.R., Chu, H.Y.,
496   Tortorici, M.A., Veesler, D., Murphy, M., et al. (2020). Protocol and Reagents for Pseudotyping
497   Lentiviral Particles with SARS-CoV-2 Spike Protein for Neutralization Assays. Viruses *12*, 513.

498   Davies, N.G., Abbott, S., Barnard, R.C., Jarvis, C.I., Kucharski, A.J., Munday, J.D., Pearson, C.A.B.,
499   Russell, T.W., Tully, D.C., Washburne, A.D., et al. (2021). Estimated transmissibility and impact
500   of SARS-CoV-2 lineage B.1.1.7 in England. Science *372*.

501   Dejnirattisai, W., Zhou, D., Ginn, H.M., Duyvesteyn, H.M.E., Supasa, P., Case, J.B., Zhao, Y.,
502   Walter, T.S., Mentzer, A.J., Liu, C., et al. (2021). The antigenic anatomy of SARS-CoV-2 receptor
503   binding domain. Cell *184*, 2183-2200.e22.

504   Deng, X., Garcia-Knight, M.A., Khalid, M.M., Servellita, V., Wang, C., Morris, M.K., Sotomayor-
505   González, A., Glasner, D.R., Reyes, K.R., Gliwa, A.S., et al. (2021). Transmission, infectivity, and
506   neutralization of a spike L452R SARS-CoV-2 variant. Cell *184*, 3426-3437.e8.

507   Elshabrawy, H.A., Coughlin, M.M., Baker, S.C., and Prabhakar, B.S. (2012). Human Monoclonal
508   Antibodies against Highly Conserved HR1 and HR2 Domains of the SARS-CoV Spike Protein Are
509   More Broadly Neutralizing. PLOS ONE *7*, e50366.

510   Emsley, P., Lohkamp, B., Scott, W.G., and Cowtan, K. (2010). Features and development of Coot.
511   Acta Crystallogr. D Biol. Crystallogr. *66*, 486–501.

512   Greaney, A.J., Starr, T.N., Gilchuk, P., Zost, S.J., Binshtein, E., Loes, A.N., Hilton, S.K., Huddleston,
513   J., Eguia, R., Crawford, K.H.D., et al. (2021a). Complete Mapping of Mutations to the SARS-CoV-
514   2 Spike Receptor-Binding Domain that Escape Antibody Recognition. Cell Host Microbe *29*, 44-
515   57.e9.

516   Greaney, A.J., Starr, T.N., Barnes, C.O., Weisblum, Y., Schmidt, F., Caskey, M., Gaebler, C., Cho,
517   A., Agudelo, M., Finkin, S., et al. (2021b). Mapping mutations to the SARS-CoV-2 RBD that
518   escape binding by different classes of antibodies. Nat. Commun. *12*, 4196.

519   Hansen, J., Baum, A., Pascal, K.E., Russo, V., Giordano, S., Wloga, E., Fulton, B.O., Yan, Y., Koon,
520   K., Patel, K., et al. (2020). Studies in humanized mice and convalescent humans yield a SARS-
521   CoV-2 antibody cocktail. Science *369*, 1010–1014.

522   Hoffmann, M., Kleine-Weber, H., Schroeder, S., Krüger, N., Herrler, T., Erichsen, S., Schiergens,
523   T.S., Herrler, G., Wu, N.-H., Nitsche, A., et al. (2020). SARS-CoV-2 Cell Entry Depends on ACE2
524   and TMPRSS2 and Is Blocked by a Clinically Proven Protease Inhibitor. Cell *181*, 271-280.e8.

525   Huo, J., Zhao, Y., Ren, J., Zhou, D., Duyvesteyn, H.M.E., Ginn, H.M., Carrique, L., Malinauskas, T.,
526   Ruza, R.R., Shah, P.N.M., et al. (2020). Neutralization of SARS-CoV-2 by Destruction of the
527   Prefusion Spike. Cell Host Microbe *28*, 445-454.e6.

528   Hutchison, C.A., Nordeen, S.K., Vogt, K., and Edgell, M.H. (1986). A complete library of point
529   substitution mutations in the glucocorticoid response element of mouse mammary tumor virus.
530   Proc. Natl. Acad. Sci. *83*, 710–714.

531   Jain, T., Sun, T., Durand, S., Hall, A., Houston, N.R., Nett, J.H., Sharkey, B., Bobrowicz, B., Caffry,
532   I., Yu, Y., et al. (2017). Biophysical properties of the clinical-stage antibody landscape. Proc.
533   Natl. Acad. Sci. *114*, 944–949.

534   Jones, B.E., Brown-Augsburger, P.L., Corbett, K.S., Westendorf, K., Davies, J., Cujec, T.P.,
535   Wiethoff, C.M., Blackbourne, J.L., Heinz, B.A., Foster, D., et al. (2021). The neutralizing antibody,
536   LY-CoV555, protects against SARS-CoV-2 infection in nonhuman primates. Sci. Transl. Med. *13*,
537   1906.

538   Kabsch, W. (2010). XDS. Acta Crystallogr. D Biol. Crystallogr. *66*, 125–132.

539   Kirchdoerfer, R.N., Cottrell, C.A., Wang, N., Pallesen, J., Yassine, H.M., Turner, H.L., Corbett, K.S.,
540   Graham, B.S., McLellan, J.S., and Ward, A.B. (2016). Pre-fusion structure of a human
541   coronavirus spike protein. Nature *531*, 118–121.

542   Kuzmina, A., Khalaila, Y., Voloshin, O., Keren-Naus, A., Boehm-Cohen, L., Raviv, Y., Shemer-Avni,
543   Y., Rosenberg, E., and Taube, R. (2021). SARS-CoV-2 spike variants exhibit differential infectivity
544   and neutralization resistance to convalescent or post-vaccination sera. Cell Host Microbe *29*,
545   522-528.e2.

546   Lai, S.-C., Chong, P.C.-S., Yeh, C.-T., Liu, L.S.-J., Jan, J.-T., Chi, H.-Y., Liu, H.-W., Chen, A., and
547   Wang, Y.-C. (2005). Characterization of neutralizing monoclonal antibodies recognizing a 15-
548   residues epitope on the spike protein HR2 region of severe acute respiratory syndrome
549   coronavirus (SARS-CoV). J. Biomed. Sci. *12*, 711–727.

550   Li, W., Moore, M.J., Vasilieva, N., Sui, J., Wong, S.K., Berne, M.A., Somasundaran, M., Sullivan,
551   J.L., Luzuriaga, K., Greenough, T.C., et al. (2003). Angiotensin-converting enzyme 2 is a
552   functional receptor for the SARS coronavirus. Nature *426*, 450–454.

553   Li, Z., Tomlinson, A.C., Wong, A.H., Zhou, D., Desforges, M., Talbot, P.J., Benlekbir, S.,
554   Rubinstein, J.L., and Rini, J.M. (2019). The human coronavirus HCoV-229E S-protein structure
555   and receptor binding. ELife *8*, e51230.

556   Liao, H.-I., Olson, C.A., Hwang, S., Deng, H., Wong, E., Baric, R.S., Roberts, R.W., and Sun, R.
557   (2009). mRNA Display Design of Fibronectin-based Intrabodies That Detect and Inhibit Severe
558   Acute Respiratory Syndrome Coronavirus Nucleocapsid Protein. J. Biol. Chem. *284*, 17512–
559   17520.

560   Lip, K.-M., Shen, S., Yang, X., Keng, C.-T., Zhang, A., Oh, H.-L.J., Li, Z.-H., Hwang, L.-A., Chou, C.-F.,
561   Fielding, B.C., et al. (2006). Monoclonal Antibodies Targeting the HR2 Domain and the Region
562   Immediately Upstream of the HR2 of the S Protein Neutralize In Vitro Infection of Severe Acute
563   Respiratory Syndrome Coronavirus. J. Virol. *80*, 941–950.

564   Liu, L., Wang, P., Nair, M.S., Yu, J., Rapp, M., Wang, Q., Luo, Y., Chan, J.F.-W., Sahi, V., Figueroa,
565   A., et al. (2020). Potent neutralizing antibodies against multiple epitopes on SARS-CoV-2 spike.
566   Nature *584*, 450–456.

567   Liu, R., Barrick, J.E., Szostak, J.W., and Roberts, R.W. (2000). Optimized synthesis of RNA-protein
568   fusions for in vitro protein selection. Methods Enzymol. *318*, 268–293.

569   Mastronarde, D.N. (2005). Automated electron microscope tomography using robust prediction
570   of specimen movements. J. Struct. Biol. *152*, 36–51.

571   McCallum, M., Bassi, J., Marco, A.D., Chen, A., Walls, A.C., Iulio, J.D., Tortorici, M.A., Navarro,
572   M.-J., Silacci-Fregni, C., Saliba, C., et al. (2021a). SARS-CoV-2 immune evasion by the
573   B.1.427/B.1.429 variant of concern. Science *373*, 648–654.

574   McCallum, M., Marco, A.D., Lempp, F.A., Tortorici, M.A., Pinto, D., Walls, A.C., Beltramello, M.,
575   Chen, A., Liu, Z., Zatta, F., et al. (2021b). N-terminal domain antigenic mapping reveals a site of
576   vulnerability for SARS-CoV-2. Cell *184*, 2332-2347.e16.

577   McCarthy, K.R., Rennick, L.J., Nambulli, S., Robinson-McCarthy, L.R., Bain, W.G., Haidar, G., and
578   Duprex, W.P. (2021). Recurrent deletions in the SARS-CoV-2 spike glycoprotein drive antibody
579   escape. Science *371*, 1139–1142.

580   McCoy, A.J., Grosse-Kunstleve, R.W., Adams, P.D., Winn, M.D., Storoni, L.C., and Read, R.J.
581   (2007). Phaser crystallographic software. J. Appl. Crystallogr. *40*, 658–674.

582   Newton, M.S., Cabezas-Perusse, Y., Tong, C.L., and Seelig, B. (2020). In Vitro Selection of
583   Peptides and Proteins—Advantages of mRNA Display. ACS Synth. Biol. *9*, 181–190.

584   Oliveira, T. de, Lutucuta, S., Nkengasong, J., Morais, J., Paixão, J.P., Neto, Z., Afonso, P.,
585   Miranda, J., David, K., Inglês, L., et al. (2021). A novel variant of interest of SARS-CoV-2 with
586   multiple spike mutations detected through travel surveillance in Africa. MedRxiv
587   2021.03.30.21254323.

588   Olson, C.A., Liao, H.-I., Sun, R., and Roberts, R.W. (2008). mRNA Display Selection of a High-
589   Affinity, Modification-Specific Phospho-IκBα-Binding Fibronectin. ACS Chem. Biol. *3*, 480–485.

590   Olson, C.A., Adams, J.D., Takahashi, T.T., Qi, H., Howell, S.M., Wu, T.-T., Roberts, R.W., Sun, R.,
591   and Soh, H.T. (2011). Rapid mRNA-Display Selection of an IL-6 Inhibitor Using Continuous-Flow
592   Magnetic Separation. Angew. Chem. Int. Ed Engl. *50*, 8295–8298.

593   Pallesen, J., Wang, N., Corbett, K.S., Wrapp, D., Kirchdoerfer, R.N., Turner, H.L., Cottrell, C.A.,
594   Becker, M.M., Wang, L., Shi, W., et al. (2017). Immunogenicity and structures of a rationally
595   designed prefusion MERS-CoV spike antigen. Proc. Natl. Acad. Sci. *114*, E7348–E7357.

596   Piccoli, L., Park, Y.-J., Tortorici, M.A., Czudnochowski, N., Walls, A.C., Beltramello, M., Silacci-
597   Fregni, C., Pinto, D., Rosen, L.E., Bowen, J.E., et al. (2020). Mapping Neutralizing and

598   Immunodominant Sites on the SARS-CoV-2 Spike Receptor-Binding Domain by Structure-Guided
599   High-Resolution Serology. Cell *183*, 1024-1042.e21.

600   Pinto, D., Park, Y.-J., Beltramello, M., Walls, A.C., Tortorici, M.A., Bianchi, S., Jaconi, S., Culap, K.,
601   Zatta, F., De Marco, A., et al. (2020). Cross-neutralization of SARS-CoV-2 by a human
602   monoclonal SARS-CoV antibody. Nature *583*, 290–295.

603   Plante, J.A., Liu, Y., Liu, J., Xia, H., Johnson, B.A., Lokugamage, K.G., Zhang, X., Muruato, A.E.,
604   Zou, J., Fontes-Garfias, C.R., et al. (2021). Spike mutation D614G alters SARS-CoV-2 fitness.
605   Nature *592*, 116–121.

606   Punjani, A., Rubinstein, J.L., Fleet, D.J., and Brubaker, M.A. (2017). cryoSPARC: algorithms for
607   rapid unsupervised cryo-EM structure determination. Nat. Methods *14*, 290–296.

608   Ribes, M., Chaccour, C., and Moncunill, G. (2021). Adapt or perish: SARS-CoV-2 antibody escape
609   variants defined by deletions in the Spike N-terminal Domain. Signal Transduct. Target. Ther. *6*,
610   1–2.

611   Robbiani, D.F., Gaebler, C., Muecksch, F., Lorenzi, J.C.C., Wang, Z., Cho, A., Agudelo, M., Barnes,
612   C.O., Gazumyan, A., Finkin, S., et al. (2020). Convergent antibody responses to SARS-CoV-2 in
613   convalescent individuals. Nature *584*, 437–442.

614   Roberts, R.W., and Szostak, J.W. (1997). RNA-peptide fusions for the in vitro selection of
615   peptides and proteins. Proc. Natl. Acad. Sci. *94*, 12297–12302.

616   Starr, T.N., Greaney, A.J., Hilton, S.K., Ellis, D., Crawford, K.H.D., Dingens, A.S., Navarro, M.J.,
617   Bowen, J.E., Tortorici, M.A., Walls, A.C., et al. (2020). Deep Mutational Scanning of SARS-CoV-2
618   Receptor Binding Domain Reveals Constraints on Folding and ACE2 Binding. Cell *182*, 1295-
619   1310.e20.

620   Starr, T.N., Greaney, A.J., Addetia, A., Hannon, W.W., Choudhary, M.C., Dingens, A.S., Li, J.Z.,
621   and Bloom, J.D. (2021). Prospective mapping of viral mutations that escape antibodies used to
622   treat COVID-19. Science *371*, 850–854.

623   Suryadevara, N., Shrihari, S., Gilchuk, P., VanBlargan, L.A., Binshtein, E., Zost, S.J., Nargi, R.S.,
624   Sutton, R.E., Winkler, E.S., Chen, E.C., et al. (2021). Neutralizing and protective human
625   monoclonal antibodies recognizing the N-terminal domain of the SARS-CoV-2 spike protein. Cell
626   *184*, 2316-2331.e15.

627   Takahashi, T.T., Austin, R.J., and Roberts, R.W. (2003). mRNA display: ligand discovery,
628   interaction analysis and beyond. Trends Biochem. Sci. *28*, 159–165.

629   Tegally, H., Wilkinson, E., Giovanetti, M., Iranzadeh, A., Fonseca, V., Giandhari, J., Doolabh, D.,
630   Pillay, S., San, E.J., Msomi, N., et al. (2021). Detection of a SARS-CoV-2 variant of concern in
631   South Africa. Nature *592*, 438–443.

632   Walls, A.C., Tortorici, M.A., Bosch, B.-J., Frenz, B., Rottier, P.J.M., DiMaio, F., Rey, F.A., and
633   Veesler, D. (2016). Cryo-electron microscopy structure of a coronavirus spike glycoprotein
634   trimer. Nature *531*, 114–117.

635   Walls, A.C., Xiong, X., Park, Y.-J., Tortorici, M.A., Snijder, J., Quispe, J., Cameroni, E., Gopal, R.,
636   Dai, M., Lanzavecchia, A., et al. (2019). Unexpected Receptor Functional Mimicry Elucidates
637   Activation of Coronavirus Fusion. Cell *176*, 1026-1039.e15.

638   Walls, A.C., Park, Y.-J., Tortorici, M.A., Wall, A., McGuire, A.T., and Veesler, D. (2020). Structure,
639   Function, and Antigenicity of the SARS-CoV-2 Spike Glycoprotein. Cell *181*, 281-292.e6.

640   Wang, P., Nair, M.S., Liu, L., Iketani, S., Luo, Y., Guo, Y., Wang, M., Yu, J., Zhang, B., Kwong, P.D.,
641   et al. (2021). Antibody resistance of SARS-CoV-2 variants B.1.351 and B.1.1.7. Nature *593*, 130–
642   135.

643   Wec, A.Z., Wrapp, D., Herbert, A.S., Maurer, D.P., Haslwanter, D., Sakharkar, M., Jangra, R.K.,
644   Dieterle, M.E., Lilov, A., Huang, D., et al. (2020). Broad neutralization of SARS-related viruses by
645   human monoclonal antibodies. Science *369*, 731–736.

646   Weinreich, D.M., Sivapalasingam, S., Norton, T., Ali, S., Gao, H., Bhore, R., Musser, B.J., Soo, Y.,
647   Rofail, D., Im, J., et al. (2021). REGN-COV2, a Neutralizing Antibody Cocktail, in Outpatients with
648   Covid-19. N. Engl. J. Med. *384*, 238–251.

649   Weisblum, Y., Schmidt, F., Zhang, F., DaSilva, J., Poston, D., Lorenzi, J.C., Muecksch, F.,
650   Rutkowska, M., Hoffmann, H.-H., Michailidis, E., et al. (2020). Escape from neutralizing
651   antibodies by SARS-CoV-2 spike protein variants. ELife *9*, e61312.

652   Widera, M., Wilhelm, A., Hoehl, S., Pallas, C., Kohmer, N., Wolf, T., Rabenau, H.F., Corman, V.,
653   Drosten, C., Vehreschild, M.J., et al. (2021). Bamlanivimab does not neutralize two SARS-CoV-2
654   variants carrying E484K in vitro. MedRxiv 10.1101/2021.02.24.21252372.

655   Winn, M.D., Ballard, C.C., Cowtan, K.D., Dodson, E.J., Emsley, P., Evans, P.R., Keegan, R.M.,
656   Krissinel, E.B., Leslie, A.G.W., McCoy, A., et al. (2011). Overview of the CCP4 suite and current
657   developments. Acta Crystallogr. D Biol. Crystallogr. *67*, 235–242.

658   Wrapp, D., Wang, N., Corbett, K.S., Goldsmith, J.A., Hsieh, C.-L., Abiona, O., Graham, B.S., and
659   McLellan, J.S. (2020). Cryo-EM structure of the 2019-nCoV spike in the prefusion conformation.
660   Science *367*, 1260–1263.

661   Wrobel, A.G., Benton, D.J., Xu, P., Roustan, C., Martin, S.R., Rosenthal, P.B., Skehel, J.J., and
662   Gamblin, S.J. (2020). SARS-CoV-2 and bat RaTG13 spike glycoprotein structures inform on virus
663   evolution and furin-cleavage effects. Nat. Struct. Mol. Biol. *27*, 763–767.

664   Yuan, M., Liu, H., Wu, N.C., Lee, C.-C.D., Zhu, X., Zhao, F., Huang, D., Yu, W., Hua, Y., Tien, H., et
665   al. (2020). Structural basis of a shared antibody response to SARS-CoV-2. Science *369*, 1119–
666   1123.

667 Yuan, M., Huang, D., Lee, C.-C.D., Wu, N.C., Jackson, A.M., Zhu, X., Liu, H., Peng, L., Gils, M.J.
668 van, Sanders, R.W., et al. (2021). Structural and functional ramifications of antigenic drift in
669 recent SARS-CoV-2 variants. Science *373*, 818–823.

670 Yuan, Y., Cao, D., Zhang, Y., Ma, J., Qi, J., Wang, Q., Lu, G., Wu, Y., Yan, J., Shi, Y., et al. (2017).
671 Cryo-EM structures of MERS-CoV and SARS-CoV spike glycoproteins reveal the dynamic
672 receptor binding domains. Nat. Commun. *8*, 15092.

673 Yurkovetskiy, L., Wang, X., Pascal, K.E., Tomkins-Tinch, C., Nyalile, T.P., Wang, Y., Baum, A.,
674 Diehl, W.E., Dauphin, A., Carbone, C., et al. (2020). Structural and Functional Analysis of the
675 D614G SARS-CoV-2 Spike Protein Variant. Cell *183*, 739-751.e8.

676 Zhou, P., Yang, X.-L., Wang, X.-G., Hu, B., Zhang, L., Zhang, W., Si, H.-R., Zhu, Y., Li, B., Huang, C.-
677 L., et al. (2020). A pneumonia outbreak associated with a new coronavirus of probable bat
678 origin. Nature *579*, 270–273.

679 Zhou, P., Yuan, M., Song, G., Beutler, N., Shaabani, N., Huang, D., He, W., Zhu, X., Callaghan, S.,
680 Yong, P., et al. (2021). A protective broadly cross-reactive human antibody defines a conserved
681 site of vulnerability on beta-coronavirus spikes. BioRxiv 10.1101/2021.03.30.437769.

682 Zivanov, J., Nakane, T., Forsberg, B.O., Kimanius, D., Hagen, W.J., Lindahl, E., and Scheres, S.H.
683 (2018). New tools for automated high-resolution cryo-EM structure determination in RELION-3.
684 ELife *7*, e42166.

685 Zost, S.J., Gilchuk, P., Case, J.B., Binshtein, E., Chen, R.E., Nkolola, J.P., Schäfer, A., Reidy, J.X.,
686 Trivette, A., Nargi, R.S., et al. (2020a). Potently neutralizing and protective human antibodies
687 against SARS-CoV-2. Nature *584*, 443–449.

688 Zost, S.J., Gilchuk, P., Chen, R.E., Case, J.B., Reidy, J.X., Trivette, A., Nargi, R.S., Sutton, R.E.,
689 Suryadevara, N., Chen, E.C., et al. (2020b). Rapid isolation and profiling of a diverse panel of
690 human monoclonal antibodies targeting the SARS-CoV-2 spike protein. Nat. Med. *26*, 1422–
691 1427.

692

693

694

695 **Materials Availability**

696 All expression plasmids generated in this study for CoV proteins, CoV pseudoviruses, human

697 Fabs and IgGs are available upon request through a MTA.

698

699   **Data availability**

700   The atomic model generated for the N-612-056 Fab complexed with SARS-CoV-2 RBD have been

701   deposited in the Protein Data Bank (PDB, http://www.rcsb.org/) under accession code 7S0B. The

702   atomic models and cryo-EM maps generated for the N-612-017, N-612-014, and N-612-004 Fabs

703   complexed with SARS-CoV-2 S have been deposited at the PDB (http://www.rcsb.org/) and the

704   Electron Microscopy Databank (EMDB) (http://www.emdataresource.org/) under accession codes

705   7S0C, 7S0D, 7S0E and EMD-24786, EMD-24787, EMD-24788, respectively. All models and

706   maps are publicly available as of the date of publication.

707

708   **Experimental Methods**

709   **mRNA display**

710   A synthetic VH3/Vk1 scFv library was transcribed by T7 run-off transcription (Thermo

711   Fisher), followed by ligation to the pF30P linker (Liu et al., 2000) via a splint oligonucleotide by

712   T4 DNA ligase (NEB). After lambda exonuclease digestion to remove splint and unincorporated

713   linker, the ligated mRNA was purified by oligo(dT)$_{25}$ dynabeads (Thermo Fisher). The mRNA-

714   puromycin template was translated (Purexpress, NEB) followed by incubation with KCl (550

715   mM final) and MgCl2 (60 mM final) for 1 hour at room temperature to enhance fusion formation

716   (Liu et al., 2000). The mRNA-scFv fusions were then affinity-purified using M2 anti-Flag beads

717   (Sigma-Aldrich) to remove non-fused template and sequences containing nonsense mutations

718   (Liao et al., 2009; Olson et al., 2011). After elution with 3XFlag peptide (Sigma-Aldrich), the

719   fusions were reverse transcribed with super script II (ThermoFisher). The pool was incubated

720   with biotinylated SARS CoV2 Spike extracellular domain bound to 5 µL streptavidin M280

721   dynabeads (ThermoFisher) for 1 hour at room temperature. After washing, the immobilized

722   fusion samples were eluted by heat (95°C) and PCR amplified with KOD hot start polymerase

723   (EMD). Affinity maturation was performed by replacing the wild type CDRs H1, H2, H3, and

724   L3 with synthetic DNA cassettes derived from oligonucleotides doped at 6% (Hutchison et al.,

725   1986) and performing 3-5 rounds of mRNA display as described above.

726   **Production antibodies and recombinant SARS-CoV-2 S domains**

727   *Molecular cloning*

728   SARS-CoV-2 Spike ECD 1-1208 (682-GSAS-685; 986-PP-987) fused to the T4 fibritin

729   trimerization domain with C-terminal Avi- and His-tag were synthesized with gene block (IDT)

730   and cloned into pcDNA.3 vector. RBD-SD1, wild type RBD and mutant RBD domains were

731   subcloned into pcDNA.3 vector with C-terminal His-tag.

732   VH and VL sequences of candidate sequences were cloned into a pcDNA.3 based vector

733   with dual CMV promotor harboring IgG1 heavy chain and light chain backbone using

734   NEBuilder Hifi DNA Assembly Master Mix (New England Biolabs).

735   *FectoPRO® transient transfection of antibodies*

736   For transient expression of antibodies by FectoPRO® transfection, CHO-S cells in

737   suspension were cultured in CD-CHO media supplemented with 8 mM L-glutamine in shaker

738   flasks at 37°C with 125 rpm rotation and 8 % CO_2. One day before transfection, CHO-S cells

739   were seeded at a density of 1 x 10^6 cells/mL in 45 mL culture flask. On the day of transfection,

740   75 µL of FectoPRO® transfection reagent (PolyPlus-transfection®) was mixed with 5 mL of 15

741   µg/mL pcDNA3 plasmid DNA harboring antibody encoding sequence in CD-CHO media and

742   incubated for 10 min at room temperature. The DNA/transfection reagent mixture was added to

743   45 mL of CHO-S culture and incubated at 37°C with 5% CO_2 and 125 rpm rotation. On Day 3,

744   50 mL of the CD-CHO media supplemented with 8 mM L-glutamine was added and the culture

745   incubated for an additional 4 days.

746   *Lipofectamine® transient transfection of RBD constructs*

747   For transient expression of RBD-SD1, RBD wild-type and RBD mutants, 293T cells were

748   cultured and and incubated at at 37°C with 5% CO_2. Plasmid harboring RBD constructs were

749   mixed with lipofectamin 2000 (Life Technology) with 1:1 (v:v) ratio and incubated for 20 min at

750   room temperature. The mixture was then added to the culture and incubated for 3-4 days.

751   *Maxcyte® transient transfection of SARS-CoV-2-S ECD trimer*

752   For transient expression of SARS-CoV-2 S di-Pro ECD timer by Maxcyte® transfection,

753   CHO-S cells were cultured in suspension in CD-CHO media supplemented with 8 mM L-

754   glutamine in shaker flasks at 37°C with 125 rpm rotation and 8% CO_2. For transfection, cells in

755   the exponential growth stage were pelleted by centrifugation at 1,400 rpm for 10 min, re-

756   suspended in 10 mL of electroporation buffer, and re-pelleted at 1,400 rpm for 5 min. The cell

757   pellet was resuspended at a density of 2 x 10^8 cells/mL in electroporation buffer, mixed with the

758   plasmid harboring SARS-CoV-2 S di-Pro ECD sequence at a concentration of 150 μg/mL, and

759   transfected using OC-400 processing assemblies in a Maxcyte® ExPERT ATx Transfection

760   System. Transfected cells were incubated for 30 min at 37°C, 5% CO_2 and then resuspended in

761   Efficient Feed A Cocktail (CHO-CD EfficientFeed™ A + 0.2% Pluronic F-68 + 1% HT

762   Supplement + 1% L-glutamine) at a density of ~4-6 x 10^6 cells/mL. This cell culture was

763   incubated at 37°C with 5% CO_2 and 125 rpm rotation overnight, 1 mM sodium buryrate was

764   added, and the culture was further incubated at 32°C with 3% CO_2 and 125 rpm for 13 more

765   days; during this incubation period, Maxcyte® Feed Cocktail (13.9% CD Hydrolysate, 69.5%

35

766   CHO CD EfficientFeed™ A, 6.2% Glucose, 6.9% FunctionMax™ Titer Enhancer, 3.5% L-

767   Glutamine) was added at 10% of the culture volume on Days 3 and Day 8.

768   *Purification of IgGs*

769   FectoPRO® transfection cell culture medium was centrifuged and filtered through a 0.22 μm

770   filter to remove cells and debris, then loaded onto a HiTrap™ MabSelect SuRe™ column (GE

771   Healthcare Life Sciences) on the AKTA Pure system pre-equilibrated with 10 mM Na Phosphate

772   and 150 mM NaCl at pH 7.0. After loading, the column was washed with 10 column volumes of

773   the same buffer. The protein was eluted with 100 mM sodium acetate, pH 3.6, then immediately

774   neutralized using 2 M Tris pH 8.0. The elution fractions were pooled and dialyzed into 10 mM

775   Hepes and 150 mM sodium chloride at pH 7.4.

776   *Purification of Fabs*

777   Fabs were generated by papain digestion using crystallized papain (Sigma-Aldrich) in 50

778   mMsodium phosphate, 2 mM EDTA, 10 mM L-cysteine, pH 7.4 for 30-60 min at 37℃ at a 1:100

779   enzyme:IgG ratio. Fab and partially cleaved IgG were applied on 1-mL HiTrap Protein L column

780   (GE Healthcare Life Science). After loading, the column was washed with 10 column volumes of

781   10 mM Na Phosphate and 150 mM NaCl at pH 7.0. The protein was eluted with 100 mM sodium

782   citrate, pH 2.5, then immediately neutralized using 2 M Tris pH 8.0. The elution fractions were

783   pooled and dialyzed into 10 mM Hepes and 150 mM sodium chloride at pH 7.4. Fabs were

784   further purified by SEC using a Superdex 200 10/300 GL column (GE Healthcare Life Sciences)

785   in 10 mM Hepes and 150 mM sodium chloride at pH 7.4.

786   *Purification of di-Pro S timer, RBD-SD1, RBD wild-type and RBD mutants*

787   The Lipofectamin transfection cell culture medium and Maxcyte transfection cell culture

788   medium was centrifuged and filtered through a 0.22 μm filter or 0.45 μm, respectively, remove

36

789   cells and debris. 50 mM Tris, 100 mM sodium chloride, and 10 mM imidazole was added to the

790   supernatant then loaded to a gravity column packed with Ni-NTA resins (Qiagen) pre-

791   equilibrated with 20 mM Tris, 300 mM sodium chloride, and 10 mM imidazole, pH 8.0. After

792   loading, the column was washed with 10 column volumes of the same buffer. The protein was

793   eluted with 20 mM Tris, 150 mM sodium chloride, and 300 mM imidazole. The elution fractions

794   were pooled and dialyzed into 10 mM Hepes and 150 mM sodium chloride, pH 7.4.

795   **Bio-Layer Interferometry (BLI) Kinetic Analysis of Antibodies**

796   BLI buffer used in all experiments was 10 mM Hepes, 150 mM NaCl, pH 7.4, with 0.02%

797   Tween 20, and 0.1% BSA. Analytes used in kinetic analysis were uncleavable S trimer, RBD-

798   SD1, RBD wild-type, RBD mutants, commercially purchased recombinant SARS-CoV-2 S2

799   (SinoBiological), and SARS-CoV-2 S1 (SinoBiological). For determining binding affinities,

800   IgGs were immobilized on Anti-hIgG Fc Capture (AHC) biosensors (Sartorius Corporation) and

801   a concentration series of 200, 100, 50, 25, 12.5, 6.25, 3.125 nM was used to determine the

802   equilibrium dissociation constants (K_D values) for RBD-SD1, RBD wild-type, RBD mutants, and

803   S1using 1:1 binding curve fit. For some RBD mutants that weakened binding and showed

804   biphasic dissociation, only 30 seconds dissociation curves were used to fit 1:1 binding model. A

805   concentration series of 20, 10, 5, 2.5, 1.25, 3.13, 1.56 nM was used to determine apparent K_D for

806   uncleavable S trimer using bivalent model on Octet HT software. For determining 1:1 binding

807   affinity for S2, S2-His-tag was immobilized on Anti-Penta-His (HIS1K) biosensors (Sartorius

808   Corporation), and a concentration series of S2 binding mAb Fab at 200, 100, 50, 25, 12.5, 6.25,

809   3.125 nM was used.

810   **ACE2 blocking assay**

811   RBD-His-tag at 5 µg/mL was first loaded on Ni-NTA (NTA) biosensors (Sartorius

812   Corporation) for 15 sec and subsequently blocked with 5 µg/mL mAbs or BLI assay buffer for 5

813   min. BLI signal from ACE2 binding were measured by incubating RBD-coated/mAb blocked

814   biosensors in 25 nM ACE2-IgG1Fc for 3 min.

815   **Epitope binning**

816   For epitope binning using S1 domain, biotinylated S1 binding mAbs at 25 µg/mL were first

817   loaded on High Precision Streptavidin SAX biosensors (Sartorius Corporation) for 10 sec. 3.75

818   µg/mL of recombinant SARS-CoV-2 S1 were used to bind mAb captured on biosensors for 3

819   min and subsequently 10 µg/mL S1 binding mAb were incubated with biosensors to observe

820   binding competition and signal was recorded for 3 min. For epitope binning using S2 domain,

821   recombinant SARS-CoV-2 S2-His-tag at 10 µg/mL was loaded on Anti-Penta-HIS (HIS1K)

822   biosensors (Sartorius Corporation) for 1 min. 10 µg/mL of S2 binding mAbs were sequentially

823   incubated with biosensors for 3-5 min to observe binding competition.

824   **Vero E6 neutralization assay**

825   All aspects of the assay utilizing virus were performed in a BSL3 containment facility

826   according to the ISMMS Conventional Biocontainment Facility SOPs for SARS-CoV-2 cell

827   culture studies. Vero E6 cells were seeded into 96-well plates at 20,000 cells/well and cultured

828   overnight at 37°C. The next day, 3-fold serial dilutions of mAbs were prepared in DMEM

829   containing 2% FBS, 1% NEAAs, and 1% Pen-Strep (vDMEM). SARS-CoV-2 virus stock was

830   prepared in vDMEM at 10,000 TCID50/mL, mixed 1:1 (v:v) with the mAb dilutions, and

831   incubated for 30 min or 24 hr at 37°C. Media was removed from the Vero E6 cells, mAb-virus

832   complexes were added and incubated at 37°C for 48 hours before fixation with 4% PFA. Fixed

833   cells were stained for SARS-CoV-2 nucleocapsid protein to measure infection. The percent

834   neutralization was calculated as 100-((sample of interest-[average of "no virus"]/[average of

835   "virus only"])*100).

836   **Pseudovirus neutralization assays**

837   Pseudoviruses based on HIV lentiviral particles were prepared as described (Robbiani et al.,

838   2020). Three-fold serially diluted mAbs were incubated with SARS-CoV-2 pseudovirus for 1

839   hour at 37°C. After incubation with 293TACE2 cells for 48 hours at 37°C, cells were washed

840   twice with PBS, lysed with Luciferase Cell Culture Lysis 5x reagent (Promega), and NanoLuc

841   Luciferase activity in lysates was measured using the Nano-Glo Luciferase Assay System

842   (Promega). Relative luminescence units (RLUs) were normalized to values derived from cells

843   infected with pseudovirus in the absence of mAbs. Half-maximal inhibitory concentrations (IC$_{50}$

844   values) for mAbs were determined using 4-parameter nonlinear regression (Prism, GraphPad).

845   **Cryo-EM sample preparation**

846   N-612-004, N-612-014 and N-612-017 Fab-S complexes were assembled by incubating

847   purified SARS-CoV-2 S trimer at a 1.1:1 molar excess of purified Fab per S protomer at RT for

848   20 min. Complex was mixed with F-octylmaltoside solution (Anatrace) to a final concentration

849   of 0.02% w/v and then 3 µL were immediately applied to a 300 mesh, 1.2/1.3 QuantiFoil grid

850   (Electron Microscopy Sciences) that had been freshly glow discharged for 30s at 20 mA using a

851   PELCO easiGLOW (Ted Pella). The grid was blotted for 3s with Whatman No. 1 filter paper at

852   22°C and 100% humidity then vitrified in 100% liquid ethane using a Mark IV Vitrobot (FEI)

853   and stored under liquid nitrogen.

854   **Cryo-EM structure determination of N-612-004, N-612-014, and N-612-017 Fab in complex**

855   **with S-6P**

856   Single-particle cryo-EM data were collected for Fab-S trimer complexes as previously

857   described (Barnes et al., 2020b) Briefly, movies were collected on a 200 kV Talos Arctica

858   transmission electron microscope (Thermo Fisher) equipped with a Gatan K3 Summit direct

859   electron detector operating in counting mode. Movies were collected using a 3x3 beam image

860   shift pattern with SerialEM automated data collection software (Mastronarde, 2005) at a nominal

861   magnification of 45,000x (super-resolution 0.4345 Å/pixel) using a defocus range of −0.7 to −2.0

862   μm. An average dose rate of 13.5 e$^-$/pix/s resulted in a total dose of ~60 e-/Å^2 over 40 frames for

863   all datasets.

864   For all datasets, movies were patch motion corrected for beam-induced motion including

865   dose-weighting within cryoSPARC v3.1 (Punjani et al., 2017)after binning super resolution

866   movies by 2 (0.869 Å/pixel). The non-dose-weighted images were used to estimate CTF

867   parameters using Patch CTF in cryoSPARC, and micrographs with poor CTF fits, signs of

868   crystalline ice, and field of views that were majority carbon were discarded. Particles were

869   picked in a reference-free manner using Gaussian blob picker in cryoSPARC(Punjani et al.,

870   2017) Initial particle stacks were extracted, binned x4 (3.48 Å/pixel), and subjected to *ab initio*

871   volume generation (4 classes) and subsequent heterogeneous refinement with all particles. The

872   3D classes that showed features for a Fab-S trimer complex or Fab-S1 protomer were 2D

873   classified to polish particle stacks. The resulting particle stacks were unbinned (0.869 Å/pixel)

874   and re-extracted using a 432 box size, and moved to Relion v3.1 (Zivanov et al., 2018) for

875   further 3D classification. Particles corresponding to distinct states were separately refined using

876   non-uniform 3D refinement imposing C1 symmetry in cryoSPARC and final resolutions were

877   estimated according to the gold-standard FSC (Bell et al., 2016).

878   To improve features at the Fab-RBD interface, focused, non-uniform 3D local refinement

879   in cryoSPARC were performed by applying a soft mask around the Fab V_HV_L – RBD (N-612-

880   017), NTD (N-612-014), or SD1 (N-612-004) domains. These efforts resulted in a modest

881   improvement in the Fab-S interface, which helped accurate model building.

882   **X-ray crystallography structure determination of N-612-056 in complex with RBD**

883   The N-612-056-RBD complex was assembled by incubating the SARS-CoV-2 RBD with

884   a 2x molar excess of Fab for 1 h on ice followed by size exclusion chromatography on an

885   superdex200 10/300 increase column (Cytiva). Fractions containing complex were pooled and

886   concentrated to 5-8 mg/mL. Crystallization trials using commercially-available screens

887   (Hampton Research) were performed at room temperature using the sitting drop vapor diffusion

888   method by mixing equal volumes of the Fab-RBD complex and reservoir using a TTP LabTech

889   Mosquito instrument. Crystals were obtained for N-612-056-RBD complex in 0.2 M Lithium

890   citrate tribasic tetrahydrate and 20% w/v polyethylene glycol 3,350, subsequently cryoprotected

891   by adding glycerol directly to drops to a final concentration of 20% v/v and cryopreserved in

892   liquid nitrogen.

893   X-ray diffraction data were collected at the Stanford Synchrotron Radiation Lightsource

894   (SSRL) beamline 12-2 on a Pilatus 6M pixel detector (Dectris). Data from single crystals were

895   indexed and integrated in XDS (Kabsch, 2010) and merged using AIMLESS in *CCP4* (Winn et

896   al., 2011)(Table S6). The N-612-056-RBD structure was solved by molecular replacement in

897   PHASER (McCoy et al., 2007) using unmodified RBD coordinates (PDB 7K8M) and

898   coordinates from C002 Fab (PDB 7K8O) as search models, after removal of C002 heavy chain

899   and light chain CDR loops. Coordinates were rigid body and B-factor refined in PHENIX v1.19

900   (Adams et al., 2010) followed by sequence matching and repeated cycles of *phenix.refine* and

901   manual building in Coot (v0.9.3) (Emsley et al., 2010) (Table S6).

Structure analyses

903   Buried surface area estimates were made using PDBePISA with a 1.4Å probe (Krissinel and

904   Henrick, 2007). Potential hydrogen bonds were assigned using a distance of <3.6A˚ and an A-D-

905   H angle of >90˚, and the maximum distance allowed for a van der Waals interaction was 4.0 Å.

906   Structure figures were made using UCSF Chimera v1.14 (Goddard et al., 2018).

907

908

909

910

911

912

913

914

915

916

917

918

919

920

921

922

923 **Supplementary Material for**

924 **Rapid Identification of Neutralizing Antibodies**

925 **against SARS-CoV-2 Variants by mRNA Display**

926 **Supplementary Methods**

927 **Developability assays**

928   *Meso Scale Diagnostics (MSD) Polyreactivity*: Six different antigens, cardiolipin (50

929 μg/mL, C0563; Sigma), KLH (5 μg/mL, H8283; Sigma), LPS (10 μg/mL, tlrl-eblps; InvivoGen),

930 ssDNA (1 μg/mL, D8899; Sigma), dsDNA (1 μg/mL, D4522; Sigma), and insulin (5 μg/mL,

931 I9278; Sigma) were coated onto MSD MULTI-Array 96-well plate (MSD) individually at 50 μL

932 per well overnight at 4°C. Plates were blocked with PBS with 0.5% BSA at room temperature

933 for 1 h, followed by three washes with PBST (PBS plus 0.05% Tween 20). Fifty microliters of

934 100 nM testing antibody solution was added to each well and incubated at RT for 1 hour

935 followed by six washes with 100 μL of PBS. Twenty microliters of 0.25 μg/mL SULFO-tag,

936 anti-Human antibody was added to the wells and incubated for 1 hour followed by six washes as

937 before. Finally, 150 μL of 2X MSD Read Buffer T (MSD) was added to each well, and

938 electrochemilluminescence signal was read by MSD Sector Imager. Polyreactivity score was

939 determined by normalizing signal by control wells with no test antibody.

940   *Hydrophobic Interaction Column (HIC):* 5 μg antibody samples (1 mg/mL) were spiked in

941 with a mobile phase A solution (1.8 M ammonium sulfate and 0.1 M sodium phosphate at pH

942 6.5) to achieve a final ammonium sulfate concentration of about 1 M before analysis. A Sepax

943 Proteomix HIC butyl-NP5 column on Agilent 1100 HPLC was used with a liner gradient of

944 mobile phase A and mobile phase B solution (0.1 M sodium phosphate, pH 6.5) over 20 min at a

945 flow rate of 1 mL/min with UV absorbance monitoring at 280 nm. Elution time was recorded.

946   *Clone Self-interaction by Bio-layer Interferometry (CSI-BLI)*: Human IgG (Sigma) was

947   loaded to an AHQ biosensor (ForteBio) to ~1 nm, followed by sensor blocking with human

948   IgG1 Fc (R&D systems). The self-association was performed at 1 µM solution concentration of

949   antibodies for 300s on an Octet Red96e system (Sartorius Corporation). The binding response

950   from the association step was subtracted from that of a reference IgG.

951   *Accelerated Stability Assay*: Antibody samples at 1 mg/mL were kept at 40°C for 30 days in

952   10 mM Hepes and 150 mM sodium chloride, pH 7.4. 10 µg of antibody was loaded onto Zenix-C

953   SEC-300 size-exclusion column (Sepax) on HPLC at Day 0, 5, 20, and 30. A long-term stability

954   slope (% aggregation/day) was calculated from the percent aggregated measured on the SEC-

955   HPLC at each time-point.

956   *Differential Scanning Fluorimetry (DSF) Analysis of Melting Temperature (Tm)*: Twenty

957   microliters of 1mg/mL antibody sample was mixed with 10 µL of 20x SYPRO Orange

958   (ThermoFisher) in a 96-well PCR plate (ThermoFisher). The plate was scanned from 40°C to

959   95°C at a rate of 0.5°C/ 2 min in a CFX96 Real-Time PCR system (Bio-Rad). The Fab Tm was

960   assigned using the first derivative of the raw data.

961   **Convalescent plasma blocking assay**

962   Spike trimer with C-terminal biotin at 5 µg/mL was first loaded on High Precision

963   Streptavidin SAX biosensors (Sartorius Corporation) for 75 min. Spike coated biosensor was

964   subsequently blocked with 10-fold diluted SARS-CoV-2 convalescent plasma for 15 min. BLI

965   signal from 10 mAbs binding to available surface of spike timer were measure by incubating

966   Spike-coated/plasma blocked biosensors in 10 µg/mL of mAbs for 3 min. BLI signal was

967   compared to self-blocking of N-612-017/N-612-017 and non-blocking pair of N-612-017/N-612-

968   004 to determine whether each mAb was completely blocked, partially blocked, or non-blocked

969   by convalescent plasma from 4 different patients.

970   **Supplementary Tables**

971

972   **Table S1. Ten unique spike binding VH/VL sequences identified by mRNA display**

Ab	CDRH1 (26-35)	CDRH2 (50-58)	CDRH3 (93-101)	CDRL3 (89-86)	
N-612-017	GFTFSSYAMH	AIWGSGSNTY	ARGRDLAAFTKTA	QQHDALPW	
N-612-056	GFTFSSYAMS	LISGSGGSTY	ARDLWGSGFFA	QQDAGTPL	RBD binder
N-612-074	GFTFSAYAMH	AIWGSGGSTY	ARDLWMAMWFG	QQRSTYPL	
N-612-004	GFTFSSYYMH	AISGSGGYTY	ARDRDHAYDWG	QQWADWPL	SD1 binder
N-612-041	GFTFSSYTMH	AISGSGGYTY	ARDRDLLWMGWA	QQYANWPL	
N-612-002	GFTFSSYTMH	AISGSGGSTY	ARDLFDWG	QQDYGFPL	NTD binder
N-612-014	GFTFSSYAMT	YISGSGGGTY	ARDRWASGWLA	QQAYAYPL	
N-612-007	GFTFSNYAMH	AISGNGGSTG	ARDRWYVKNA	QQLDGTPF	
N-612-044	GFTFSNYAMH	AISGSGGSTY	ARDLSFWLTYHLASA	QQSYSDPL	S2 binder
N-612-086	GFTFSSYAMH	AISWSGRSTY	ARDLSSNWGSG	QQSADTPF	

973

974   **Table S2. BLI kinetic parameters obtained for various SARS-CoV-2 Spike domains (RBD,**

975   **RBD-SD1, S1, S2)**

Analyte	nAb	k_{on} (1/Ms)	k_{off} (1/s)	K_D (nM)
RBD	N-612-017	6.77E+05	3.58E-03	5.29
	N-612-056	3.37E+05	1.01E-03	2.98
	N-612-074	1.33E+05	1.48E-03	11.1
RBD-SD1	N-612-017	4.56E+05	3.94E-03	8.65
	N-612-056	3.59E+05	1.04E-03	2.89
	N-612-074	1.21E+05	3.97E-03	32.9
	N-612-004	1.51E+05	9.79E-04	6.49
	N-612-041	2.10E+05	3.35E-03	16.0
S1	N-612-017	2.77E+05	2.04E-03	7.37
	N-612-056	1.51E+05	5.86E-04	3.89
	N-612-074	1.01E+05	1.46E-03	14.4
	N-612-004	9.92E+04	2.13E-04	2.15
	N-612-041	1.25E+05	1.83E-03	14.4
	N-612-002	2.68E+05	7.26E-04	2.71
	N-612-014	1.76E+05	2.18E-03	12.4
S2 (Ligand)	N-612-007 (Fab)	3.70E+05	1.40E-03	3.79
	N-612-044 (Fab)	1.70E+05	1.61E-03	9.44
	N-612-086 (Fab)	2.67E+05	0.96E-02	11.6

976

45

977   **Table S3. BLI kinetic parameters obtained for Spike trimer using bivalent model fit**

Ab	k_{on1} (1/Ms)	k_{on2} (1/Ms)	k_{off1} (1/s)	k_{off2} (1/s)	Apparent K_D (nM)
N-612-017	8.35E+04	1.55E+00	<1.0E-07	1.69E-02	<0.001
N-612-056	6.24E+04	1.94E+00	<1.0E-07	5.15E-02	<0.001
N-612-074	9.23E+04	8.12E-01	<1.0E-07	1.89E-01	<0.001
N-612-004	7.60E+04	4.24E+00	<1.0E-07	1.00E+00	<0.001
N-612-041	1.11E+05	4.06E-01	<1.0E-07	1.75E-01	<0.001
N-612-002	5.69E+04	6.82E-02	<1.0E-07	6.76E-02	<0.001
N-612-014	2.54E+04	3.82E-03	2.29E-07	2.82E+00	0.0033
N-612-007	5.78E+04	7.80E-02	<1.0E-07	2.92E-02	<0.001
N-612-044	7.15E+04	2.62E+00	<1.0E-07	7.14E-02	<0.001
N-612-086	6.11E+04	1.55E-01	<1.0E-07	5.53E-02	<0.001

978

979   **Table S4. Developability assay summary table**

Ab	Polyreactivity MSD (Fold-over-PBS)	HIC (min)	BLI-CSI (nm)	Accelerated stability % monomer increase/day	Fab Tm (℃)
N-612-017	3	10.1	-0.06	0.09	85
N-612-056	7	11.5	0.00	0.10	81
N-612-074	31	**22.1**	-0.01	0.10	76
N-612-004	14	14.9	0.05	0.13	85
N-612-041	10	**20.4**	0.05	**0.37**	88
N-612-002	22	13.9	0.08	0.18	82
N-612-014	4	12.3	0.09	0.16	88
N-612-007	10	11.8	0.04	0.11	82
N-612-044	8	**13.4/15.4**	-0.06	0.10	88/91
N-612-086	10	13.2	0.07	0.11	88
Acceptance criteria	<50	<16	<0.2	<0.2	>65 ℃

980

981

982   **Table S5. Cryo-EM data collection and refinement statistics (related to Figures 3 and 5).**

	N-612-017 Fab SARS-CoV-2 S 6P	N-612-014 Fab SARS-CoV-2 S 6P	N-612-004 Fab SARS-CoV-2 S 6P
PDB	**7S0C**	**7S0D**	**7S0E**
EMD	**24786**	**24787**	**24788**
Data collection conditions			
Microscope	Talos Arctica	Talos Artica	Talos Arctica
Camera	Gatan K3 Summit	Gatan K3 Summit	Gatan K3 Summit
Magnification	45,000x	45,000x	45,000x
Voltage (kV)	200	200	200
Recording mode	counting	counting	counting
Dose rate (e$^-$/pixel/s)	13.5	13.3	13.8
Electron dose (e$^-$/Å^2)	60	60	60
Defocus range (μm)	0.7 – 2.0	0.7 – 2.0	0.7 – 2.0
Pixel size (Å)	0.8689	0.8689	0.8689
Micrographs collected	2,585	3,791	3,717
Micrographs used	2,132	3,211	2,047
Total extracted particles	282,890	505,695	595,163
Refined particles	175,986	389,223	115,068
Particles in final refinement	108,746	137,684	107,271
Symmetry imposed	C1	C1	C1
FSC 0.143 (unmasked/masked)			
unmasked	4.4 Å	6.4 Å	7.1 Å
masked	3.2 Å	3.5 Å	4.8 Å
Refinement and Validation			
Initial model used	6XKL	6XKL	6XKL
Number of atoms			
Protein	29,164	33,650	5,307
Ligand	434	873	28
MapCC (global/local)	0.81/0.78	0.79/0.76	0.87/0.69
Map sharpening B-factor	65.8	75.3	155
R.m.s. deviations			
Bond lengths (Å)	0.01	0.005	0.02
Bond angles (˚)	0.9	0.89	1.5
MolProbity score	2	2.2	2.46
Clashscore (all atom)	13.4	17.7	7.9
Poor rotamers (%)	0.2	0.1	0
Ramachandran plot			
Favored (%)	94.7	93.4	92.8
Allowed (%)	5.1	6	6.3
Disallowed (%)	0.2	0.6	0.9

983
984
985

986 **Table S6. X-ray crystallography data collection and refinement statistics (related to Figure**
987 **4).**

	N-612-056 - SARS2-RBD (12-2, SSRL)
PDB ID	**7S0B**
Data collection[a]	
Space group	$P2_12_12$
Unit cell (Å)	102.3, 153.7, 96.6
α, β, γ (°)	90, 90, 90
Wavelength (Å)	0.979
Resolution (Å)	38.9-29 (3.04-2.9)
Unique Reflections	34,420 (4,471)
Completeness (%)	99.8 (99.1)
Redundancy	6.6 (6.7)
$CC_{1/2}$ (%)	99.3 (72.8)
$<I/\sigma I>$	6.4 (1.5)
Mosaicity (°)	0.25
R_{merge} (%)	18.7 (133)
R_{pim} (%)	8.3 (59.4)
Wilson B-factor	56.6
Refinement and Validation	
Resolution (Å)	384 - 2.9
Number of atoms	
Protein	9,829
Ligand	28
Waters	0
R_{work}/R_{free} (%)	212/25.4
R.m.s. deviations	
Bond lengths (Å)	0.006
Bond angles (°)	1.2
MolProbity score	2.47
Clashscore (all atom)	11.6
Poor rotamers (%)	5
Ramachandran plot	
Favored (%)	94.8
Allowed (%)	5.2
Disallowed (%)	0
Average B-factor (Å)	73.5

[a]Numbers in parentheses correspond to the highest resolution shell

988
989

Table S7. BLI kinetic analysis of N-612-017, N-612-017-01, N-612-017-03, N-612-017-5B02, and N-612-017-5B05 against RBD-WT, RBD-B.1.351 (K417N/E484K/N501Y) and RBD-L452R

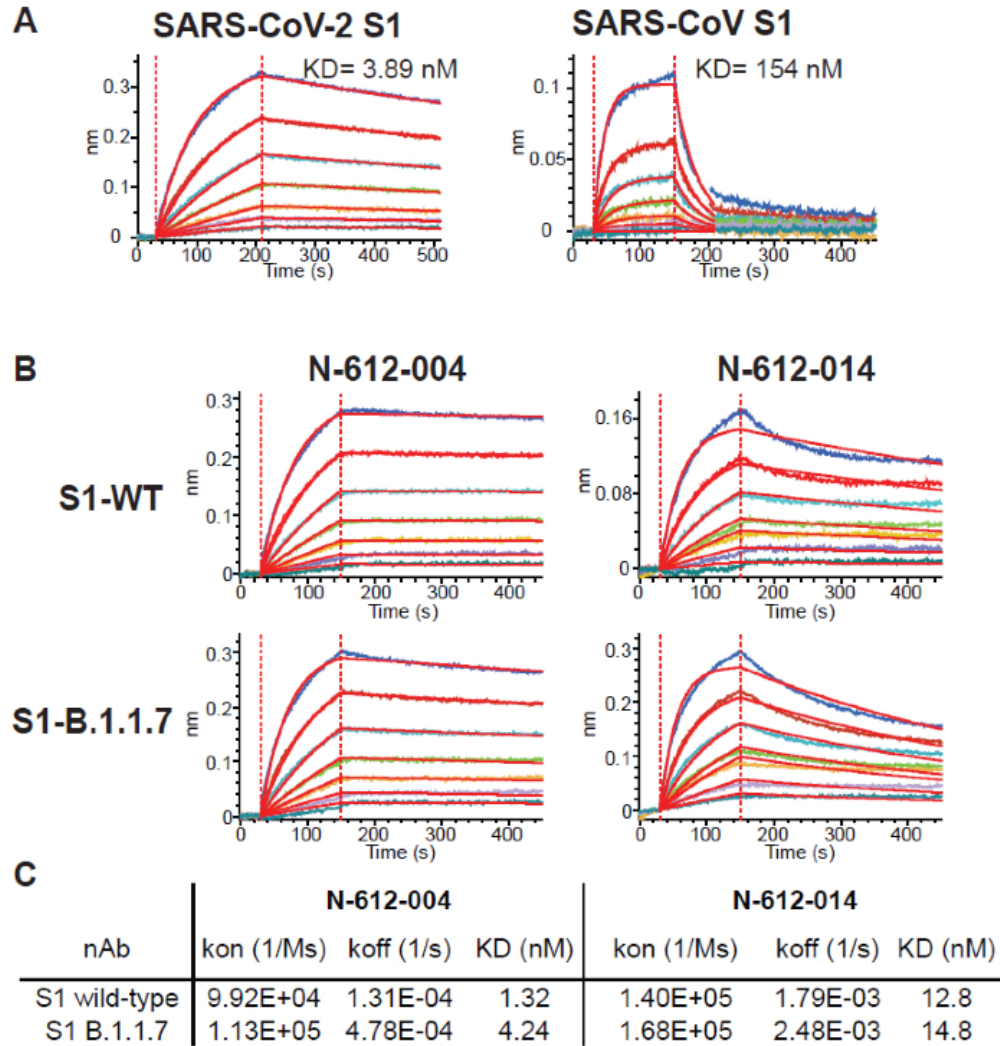|	RBD-WT			RBD-B.1.351			RBD-L452R		
	k_{on} (1/Ms)	k_{off} (1/s)	K_D (nM)	k_{on} (1/Ms)	k_{off} (1/s)	K_D (nM)	k_{on} (1/Ms)	k_{off} (1/s)	K_D (nM)
N-612-017	6.77E+05	3.58E-03	5.29	4.45E+05	1.36E-02	30.6	--	--	N.B.
N-612-017-01	5.59E+05	3.59E-04	0.64	5.31E+05	4.06E-04	0.77	2.34E+05	7.75E-03	33.1
N-612-017-03	6.48E+05	1.60E-04	0.25	6.47E+05	2.33E-04	0.36	1.18E+05	6.90E-03	58.7
N-612-017-5B02	8.24E+05	9.26E-05	0.11	7.99E+05	1.20E-04	0.15	5.74E+05	3.54E-03	6.16
N-612-017-5B05	9.62E+05	3.16E-03	3.28	9.68E+05	2.48E-03	2.56	8.01E+05	1.96E-03	2.44
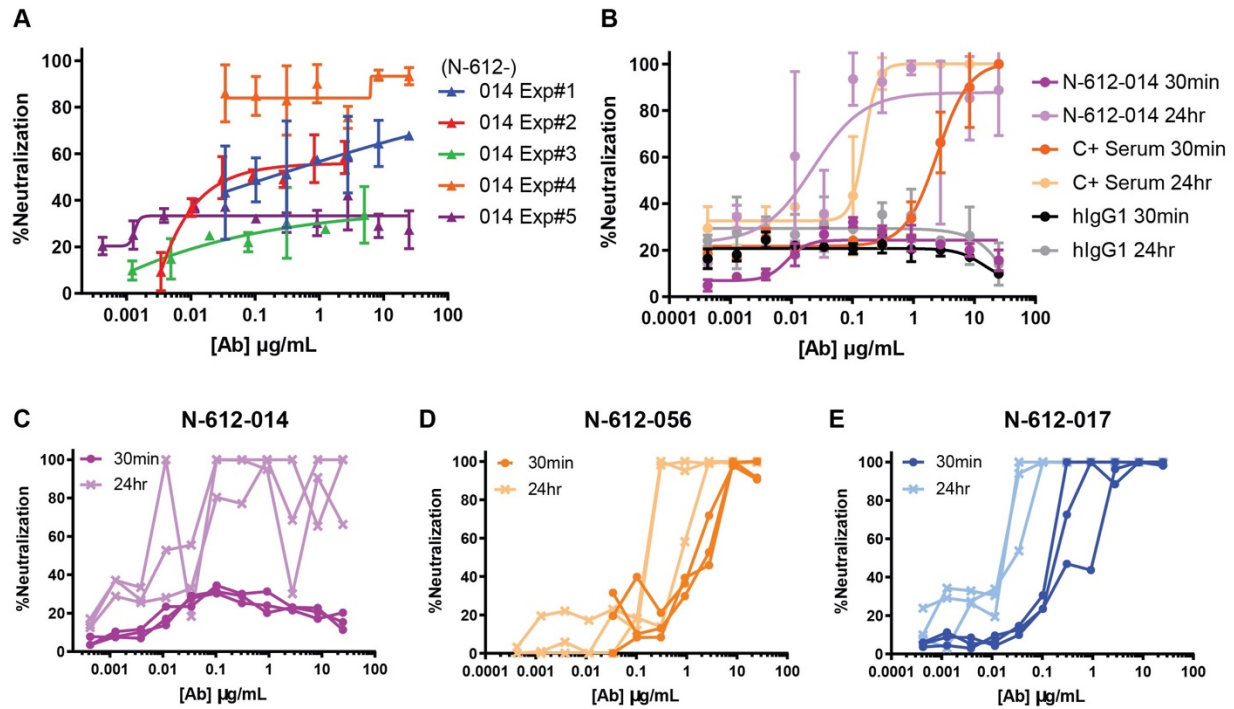
Figure S1. Vero E6 live virus neutralization assay (A) Neutralization activity of N-612-014 in 5 separate experiments. (B) Comparison of neutralization activity of N-612-014, convalescent (C+) serum, and control human IgG with 30-min vs 24-hr antibody-virus incubation. (C, D, E) Change in neutralization potency by incubation time.
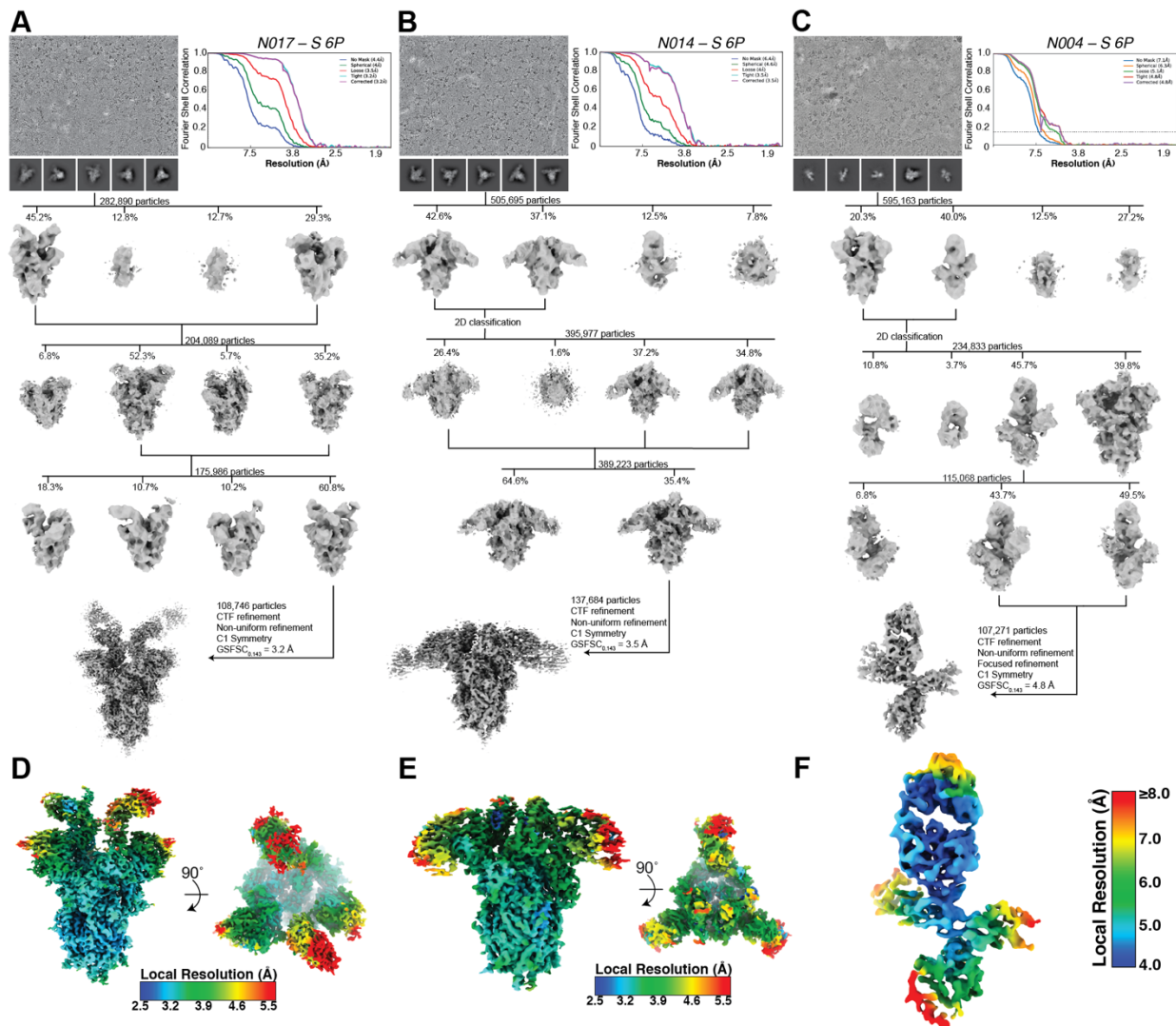
1036
1037 **Figure S2. Cryo-EM data processing and validation (related to Figures 3 and 5).** (A-C)
1038 Representative micrograph, 2D class averages, data processing workflow, and Gold Standard
1039 FSC plots for the final reconstructions of (A) N-612-017 – S 6P, (B) N-612-014 – S 6P, and (C)
1040 N-612-056 – S 6P complexes. (D-F) Local resolution estimates calculated in cryoSPARC v3.1
1041 for (D) N-612-017 – S 6P, (E) N-612-014 – S 6P, and (F) N-612-056 – S 6P complexes.

A SARS-CoV-2 S1, KD= 3.89 nM; SARS-CoV S1, KD= 154 nM

B N-612-004 and N-612-014 (S1-WT and S1-B.1.1.7)

C

nAb	N-612-004			N-612-014		
	kon (1/Ms)	koff (1/s)	KD (nM)	kon (1/Ms)	koff (1/s)	KD (nM)
S1 wild-type	9.92E+04	1.31E-04	1.32	1.40E+05	1.79E-03	12.8
S1 B.1.1.7	1.13E+05	4.78E-04	4.24	1.68E+05	2.48E-03	14.8

Figure S3: (A) Cross-reactivity of N-612-056 against SARS-CoV. BLI kinetic analysis of SARS-CoV-2 and SARS-CoV S1 domain binding to N-612-056. (B, C) BLI kinetic analysis of N-612-004 and N-612-014 against S1 domain from WT and B.1.1.7 variant of SARS-CoV-2 Spike protein.

	EX1	EX2	EX3	EX4
No blocking	004(SD1) 041(SD1) 056(RBD)	004(SD1) 041(SD1) 056(RBD)	004(SD1) 041(SD1) 056(RBD)	004(SD1) 041(SD1)
Partial Blocking	002(NTD) 014(NTD) 017(RBD) 074(RBD)	002(NTD) 014(NTD) 017(RBD) 074(RBD)	002(NTD) 014(NTD) 017(RBD) 074(RBD)	002(NTD) 014(NTD) 017(RBD) 056(RBD) 074(RBD)
Blocking	007(S2) 044(S2) 086(S2)	007(S2) 044(S2) 086(S2)	007(S2) 044(S2) 086(S2)	007(S2) 044(S2) 086(S2)

1051

1052 **Figure S4. Convalescent plasma blocking of 10 mAbs binding to SARS-CoV-2 Spike.**

1053

1054
1055